Important Notice

UNIVERSITY OF CALGARY

Seismic imaging using matched filters for operator weighting

by

Jeffrey Karl Beckett

A THESIS

SUBMITTED TO THE FACULTY OF GRADUATE STUDIES

IN PARTIAL FULFILMENT OF THE REQUIREMENTS FOR THE

DEGREE OF MASTER OF SCIENCE

DEPARTMENT OF GEOLOGY AND GEOPHYSICS

CALGARY, ALBERTA

AUGUST, 2004

UNIVERSITY OF CALGARY

FACULTY OF GRADUATE STUDIES

The undersigned certify that they have read, and recommend to the Faculty of Graduate

Studies for acceptance, a thesis entitled "Seismic imaging using matched filters for

operator weighting" submitted by Jeffrey Karl Beckett in partial fulfilment of the

requirements of the degree of Master of Science.

_____
Supervisor, Dr. J.C. Bancroft, Department of Geology and Geophysics

_____
Dr. L.R. Lines, Department of Geology and Geophysics

_____
Dr. J. A. Blais, Department of Geomatics Engineering

_____
Date

Abstract

Given a particular statistical measure of signal to noise (S/N), the 'matched filter' is an ideal linear filter for maximizing the S/N ratio of a signal amongst random, white noise. A matched filter approach to event detection in prestack migration is proposed, where 'signal' is defined as a particular amplitude variation with offset (AVO) reflection coefficient surface, and all other AVO response surfaces are considered 'noise'. Matched filtering of the prestack data with the signal illuminates reflection events whose AVO response curve matches that of the signal; other reflection energy is suppressed. Matched filter imaging enhances the detection of Class 2 AVO events, and results in an overall S/N improvement over conventional P-SV wave prestack migration.

Acknowledgements

Dedication

For Bill

Table of Contents

List of Figures

x

List of Symbols and Abbreviations

AGC   Automatic Gain Control

AVO   Amplitude Variation with Offset

CDP   Common Depth Point

CMP   Common MidPoint

CREWES   Consortium for Research in Elastic Wave Exploration Sesimology

DSR   Double Square Root

EO   Equivalent Offset

EOCP   Equivalent Offset Conversion Point

NMO   Normal MoveOut

OBS   Ocean Bottom Cable

RC   Reflection Coefficient

RMS   Root Mean Square

SNR   Signal to Noise Ratio

P   Primary, or compressional wave

P-P   P-to-P seismic reflection

P-SV   P-to-SV seismic reflection

S   Secondary, or shear wave

SV   S wave whose particle motion is parallel to source-receiver plane

V_P P-wave velocity

V_{Pmig} effective P-wave migration velocity

V_{Smig} effective S-wave migration velocity

V_S	S-wave velocity
dr	radial distance from scatterpoint to receiver
ds	radial distance from source to scatterpoint
h	half of the source-receiver offset
h_e	equivalent offset
h_s	horizontal distance from scatterpoint surface location to souce location
h_r	horizontal distance from scatterpoint surface location to receiver location
t_r	traveltime from scatterpoint to receiver
t_s	traveltime from source to scatterpoint
z_0	depth of scatterpoint
α	compressional velocity of a medium
β	shear velocity of a medium
γ_{mig}	V_{Pmig}/V_{Smig} ratio
ρ	density of a medium
σ	Poisson's ratio
θ_1	P-wave incident angle
μ	Signal-to-noise ratio

Chapter 1: Introduction

1.1 Background

The accurate imaging of subsurface geology from surface-acquired seismic data is one of the chief challenges of exploration geophysics. A reflection seismic experiment essentially involves sending an impulse into the Earth, where the elastic wavefield is reflected from various interfaces, and finally recorded at the surface. The seismic data may be conditioned through the processes of random noise suppression, frequency content recovery, and the removal of near surface effects, but the data are ultimately placed back their appropriate geological positions through the process of migration.

The relative amplitude of a P-P wave reflection event depends on the change in rock properties across a given interface, and the reflection incidence angle, θ. The term 'reflection coefficient' is defined as the ratio of the amplitude of the reflected wave to the amplitude of the incident wave. Governed by the Zoeppritz equations, the reflection coefficient is a function of θ and the elastic Earth parameters (compressional velocity, V_P, shear velocity, V_S, and density, ρ) of the media across the interface. Due to the nature of this physical process, some geologic interfaces will produce greater amplitude events than others, and it is often the weaker events that are of interest to image. Given a shale/porous sand interface, Ostrander (1982) showed that reflection amplitudes varied anomalously with increasing source/receiver offset, and demonstrated how to apply this discovery to the detection of hydrocarbons. Ostrander's work spawned the field of study

of what has become known as "amplitude variation with offset" (AVO). As the change in elastic Earth properties across an interface determine the AVO response of the reflection, we can enhance, or suppress, the relative strength of the event based on its AVO response through the process of matched filtering.

Given a particular statistical measure of signal-to-noise, the "matched filter" is the ideal linear filter for maximizing the signal-to-noise ratio (SNR) of a signal amongst random, white noise. A matched filter approach to event detection in pre-stack migration is proposed, where 'signal' is defined as a particular AVO reflection coefficient surface, and all other AVO response surfaces are considered 'noise'. This project shows how crosscorrelation of the pre-stack data with the desired signal illuminates reflection events whose AVO response curve matches that of the signal, while other reflection energy is suppressed. Matched filter imaging enhances the detection of Class II AVO events.

Consider a compressional wave (P-wave) that reflects off of an arbitrary interface. Some of this reflected energy will propagate as shear waves (S-waves). These mode-converted waves are referred to as P-S waves. A shear wave whose particle motion is in the CMP-depth plane is termed a P-SV wave, where the 'V' signifies 'vertical component'. Matched filtering results in an overall S/N improvement over conventional P-SV wave pre-stack migration. Two matched filter based approaches to enhanced event detection in pre-stack migration are presented in this thesis.

1.2 Thesis objectives and structure

This thesis presents two chief imaging problems. First, there is a category of low impedance contrast events that change polarity with increasing offset (Class II AVO event). Stacking results in a poor image of the event due to destructive interference. Second, the amplitude of the reflection coefficients of P-SV waves approach zero as the offset approaches zero. Consequently, near-offset data are generally dominated by noise. The objective is to demonstrate how matched filtering and AVO may be applied to enhance SNR in P-SV pre-stack migration. Focus is placed on the detection of low impedance contrast Class II AVO events, and the overall SNR in P-SV pre-stack migration.

This work is divided into three sections. Chapter 2 presents an overview of AVO, matched filters, and the equivalent offset method of pre-stack migration (EOM). In addition, a discussion is provided describing how these tools are synthesized to yield outputs with enhanced event detection. A case study for the application of this method on both synthetic and real P-P wave data is given in Chapter 3.

Similarly, a P-SV wave case study is described in Chapter 4.

1.3 Data sets used

Synthetic and real field data sets used to test the migration algorithms are discussed below.

- Synthetic data sets: All synthetic data were generated in MATLAB. Details concerning the model and the acquisition parameters are discussed in Chapters 3 and 4.

- Blackfoot 2D field data set: This data set was used to test the P-SV matched filter algorithm.

- Alba 3D field data set: The P-P wave matched filter algorithms were tested on an inline of CDPs extracted from this data set.

1.4 Software and Hardware used

The research was developed on a SUN Microsystems network operated by CREWES at the University of Calgary. All of the routines used to generate the synthetic data were coded in MATLAB. The following routines were coded in C, using Seismic UNIX (SU) as a platform.

The processing (i.e. filtering, NMO correction, deconvolution and post-stack migrations) was performed using the ProMAX processing package.

1.5 Contributions of this thesis

The main contributions in this thesis may be introduced as follows:

- Matched filter theory was successfully applied to improve the imaging of seismic data.

- By considering a particular AVO response to be 'signal', crosscorrelation of the seismic data with the 'signal' enhances the imaging of events whose AVO response most closely match the signal.

- Matched filtering of P-P wave data with a linear ramp function is a simple and effective way to enhance the detection of events that exhibit AVO behavior.

- Class II AVO events demonstrate the most dramatic improvement in image enhancement though matched filtering with a ramp function.

- Matched filtering P-SV wave data with an arbitrary P-SV AVO response curve serves as an effective near-offset noise attenuator, thus improving velocity analysis and enhancing the imaging of the output section.

The following software was coded in C, using Seismic UNIX (SU) as a platform.

- Conventional 3D P-P wave Equivalent Offset (EO) Kirchhoff prestack migration

- Conventional 2D P-SV wave EO Kirchhoff prestack migration

- 3D P-P wave matched filter EO Kirchhoff prestack migration

- 2D P-SV wave matched filter EO Kirchhoff prestack migration

- Zoeppritz equation solver

- Angle of incidence estimators, for P-P and P-SV wave

Chapter 2: Theory

2.1 Introduction

      This chapter is divided in two sections: 1) a general overview of EO Kirchhoff prestack migration, AVO analysis, and matched filtering are given as they are the central principles to this thesis, and 2) the methodology behind the application of these concepts to matched-filtered prestack migration.

2.2 Kirchhoff Pre-stack migration kinematics

      Consider a 2-D seismic survey, and the associated prestack geometry found in Figure 2.1., where h is half of the source-receiver offset, z_0 is the depth of the scatterpoint, and x is the distance between the midpoint and surface scatterpoint location.
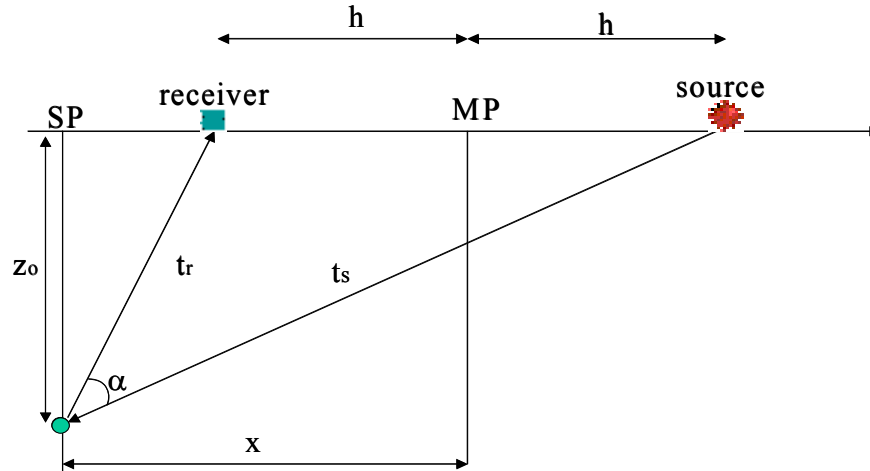
Fig. 2.1. Prestack time migration geometry showing traveltime from source to scatterpoint, t_s, and traveltime from scatterpoint to receiver, t_r.

In Kirchhoff theory, the subsurface is assumed to be composed of scatterpoints that scatter energy from any source to all receivers (Schneider, 1978). A seismic reflection event occurs when a structured arrangement of scatterpoints produce a coherent reflection. The purpose of Kirchhoff prestack migration is to sum the energy along the traveltime surface of each scatterpoint and place the energy back at the scatterpoint location, in accordance with the Kirchhoff integral (Hubral et al., 1996). This procedure is repeated for each scatterpoint within the prestack volume.

The total traveltime, t, from source to scatterpoint, t_s, and from scatterpoint to receiver, t_r, in isotropic, constant velocity media is given by (Bancroft *et al.*, 1998):

$$t = t_s + t_r. \tag{2.1}$$

From the geometry of Figure 2.1, the terms t_s and t_r may be expanded to give the Double Square Root (DSR) equation (Bancroft *et al.*, 1998) where

$$t_s = \left(\frac{z_0^2 + (x+h)^2}{V_P^2} \right)^{1/2},$$ (2.2)

and

$$t_r = \left(\frac{z_0^2 + (x-h)^2}{V_P^2} \right)^{1/2},$$ (2.3)

yielding

$$t = \left(\frac{z_0^2 + (x+h)^2}{V_p^2} \right)^{1/2} + \left(\frac{z_0^2 + (x-h)^2}{V_P^2} \right)^{1/2}.$$ (2.4)

where V_P is the P-P wave velocity, and is constant. The shape of this P-P wave energy traveltime surface is often referred to as "Cheops pyramid" (Ottolini, 1982), due to its resemblance to the ancient Egyptian King's tomb. An example of Cheops pyramid is shown in Figure 2.2.

To approximately handle vertical velocity variations and weak velocity variations, the DSR equation can be modified to give

$$t = \left(\left(\frac{t_0}{2} \right)^2 + \frac{(x+h)^2}{V_{Pmig}^2} \right)^{1/2} + \left(\left(\frac{t_0}{2} \right)^2 + \frac{(x-h)^2}{V_{Pmig}^2} \right)^{1/2},$$ (2.5)

where V_{Pmig} is the RMS approximation of Taner and Koeler (1969) evaluated at t_0. The time t_0 is the two way zero-offset time computed from the average velocity V_{ave} by

$$t_0 = \frac{2z_0}{V_{ave}}.$$ (2.6)

Consider now the P-SV wave energy traveltime surface of a scatterpoint. The traveltime surface is again given by the DSR equation; however, it is a modified version

of equation (2.4) as it incorporates the shear wave velocity for the scatterpoint-receiver ray path. The P-SV wave DSR equation is now given by:

$$t = \left(\frac{z_0^2 + (x+h)^2}{V_{Pmig}^2} \right)^{1/2} + \left(\frac{z_0^2 + (x-h)^2}{V_{Smig}^2} \right)^{1/2} , \qquad (2.7)$$

where V_{Smig} is the shear wave velocity. An example of a P-SV wave energy traveltime surface can be found in Figure 2.3.

a)

b)
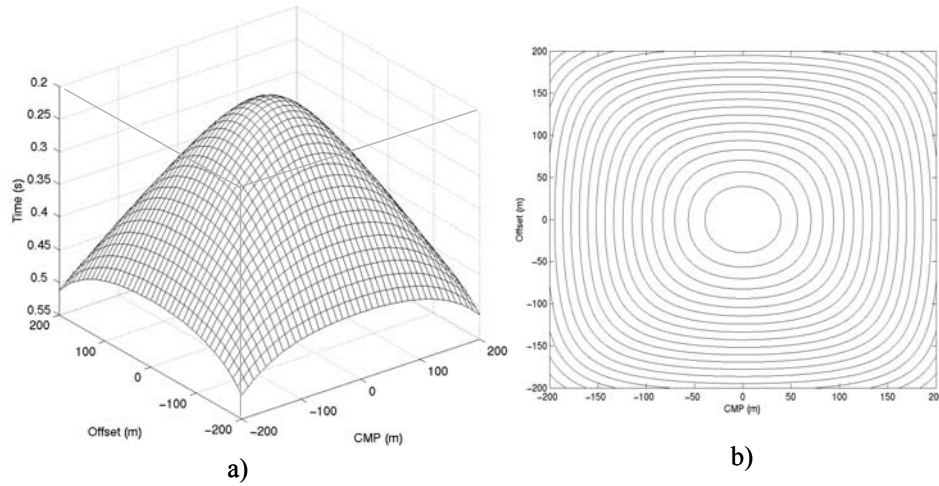
Fig. 2.2. a) Perspective view of a P-P wave traveltime surface for a scatterpoint located at z_0.=100m and V_P =800m/s b) Plan view of (a) showing contour lines of constant traveltimes.
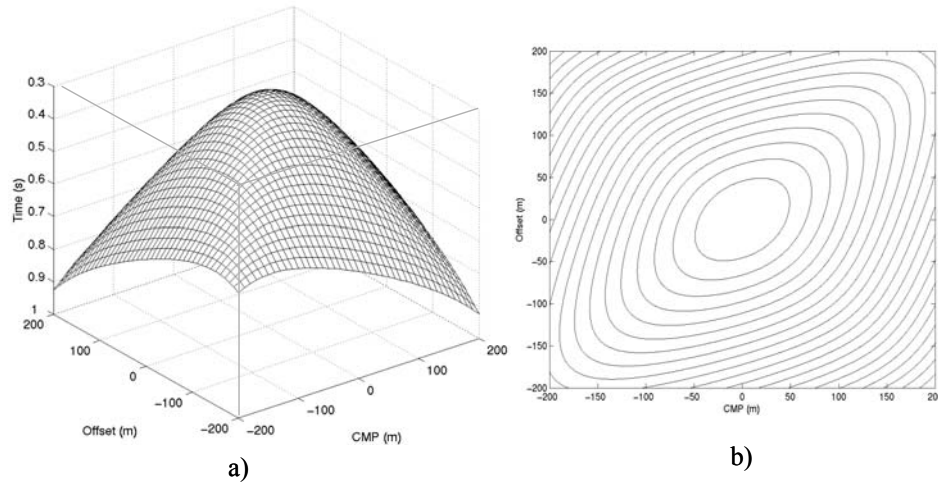
Fig. 2.3. a) Perspective view of a P-SV wave traveltime surface for a scatterpoint located at z_o=100m. V_P=800m/s, and V_S=400m/s. b) Plan view of (a) showing contour lines of constant traveltimes.

Observe that the converted wave traveltime surface (Figure 2.3) differs from the P-P case (Figure 2.2) in that it appears to be biased along the line $h=x$. This shape change is due to the asymmetry of P-SV wave raypaths. Conventional Kirchhoff prestack migration involves summing over the scatterpoint energy traveltime surface and placing energy back at the appropriate scatterpoint location. This procedure is repeated for all of the scatterpoints in the pre-stack volume. Corrections are made to compensate for spherical divergence, obliquity, and wavelet distortion (Bancroft, 2000).

2.3 EOM

The Equivalent Offset Method (EOM) of prestack time migration is computationally fast and provides excellent velocity information. This technique is based on and includes

all of the benefits of Kirchhoff time prestack migration, and may be applied to both P-P

wave and P-SV data (Bancroft *et al*.,1998). EOM is thus chosen for the analysis.

EOM is founded on the principles of equivalent offsets and equivalent offset (EO)

gathers. The equivalent offset is used to enable the gathering of input samples prior to

any time shifting. Equivalent offsets are chosen such that the total traveltime from source

to receiver, t, is equal to that of a co-located source and receiver, $2t_e$, as shown in Figure

2.4, where h_e is the equivalent offsets from the surface scatterpoint location. The EO

gathers are scaled, filtered and corrected for normal moveout (NMO). Stacking of the EO

gather produces the output prestack migrated trace.

Fig. 2.4. The position of the equivalent offset and traveltimes for a scatterpoint.

2.3.1. EOM migration of P-P wave data

Through defining this new equivalent position offset E, the traveltime equation (2.1) becomes

$$t = 2t_e = t_s + t_r.$$ (2.8)

and equation (2.3) is modified to incorporate the equivalent traveltimes to become

$$2\left(\left(\frac{t_0}{2}\right)^2 + \frac{h_e^2}{V_{Pmig}^2}\right)^{1/2} = \left(\left(\frac{t_0}{2}\right)^2 + \frac{(x+h)^2}{V_{Pmig}^2}\right)^{1/2} + \left(\left(\frac{t_0}{2}\right)^2 + \frac{(x-h)^2}{V_{Pmig}^2}\right)^{1/2}.$$ (2.9)

Solving equation (2.9) for the equivalent offset, h_e, yields (Bancroft *et al.*, 1997)

$$h_e^2 = x^2 + h^2 - \left(\frac{2xh}{tV_{mig}}\right)^2$$ (2.10)

This result is significant as the two square root terms of equation (2.9) have been collected into a single square root term. As the traveltimes have not been changed, EOM maps the data to EO gathers with no time shifting, thus limiting the migration time shift solely to a hyperbolic moveout correction on the EO gathers.

Assuming that the traveltimes are independent of the azimuthal direction of raypaths, EOM can be applied to 3D data by defining new variables, x' and h', such that

$$h' = \frac{ds + dr}{2},$$ (2.9)

and

$$x' = \frac{|ds - dr|}{2},$$ (2.10)

where *ds* and *dr* are the radial distances from source to scatterpoint surface location, and scatterpoint surface location to receiver, respectively. This 3D generalization of EOM is used in the migration of the Alba data, which is discussed in chapter 3.

2.3.2 EOM migration of P-SV wave data

The formation of converted wave data into equivalent offset conversion points (EOCP) is slightly more complicated and expensive due to the asymmetry of converted wave raypaths. However, Wang (1997) showed that the P-SV DSR equation (2.5) could be reorganized such that the equivalent offset, h_e, is given by

$$h_e = \left[\frac{T^2 V_{Pmig}^2}{\left(1+\gamma_{mig}\right)^2} - Z_0^2 \right]^{1/2}, \tag{2.11}$$

where the migration velocity ratio is defined as

$$\gamma_{mig} = \frac{V_{Pmig}}{V_{Smig}}, \tag{2.12}$$

and the pseudo depth, Z_0 is given by

$$Z_0^2 = \frac{C_2^2 - 2C_1 \pm C_2 \left(C_2^2 + 4h_s^2 - 4C_1\right)^{1/2}}{2} \tag{2.13}$$

where C_1 and C_2 are coefficients given by

$$C_1 = \frac{T^2 V_{Pmig}^2 + h_s^2 - \gamma_{mig}^2 h_r^2}{1 - \gamma_{mig}^2}$$

and

$$C_2 = \frac{TV_{Pmig}}{1 - \gamma_{mig}^2}.$$

As shown in Figure 2.5, h_s, h_r, and h_e are the source, receiver, and equivalent offsets from the EOCP surface location respectively. As with the previous P-P wave case, the above equations can be used to gather prestack P-SV wave data without any time shifting. Again, normal moveout correction and stacking of these EOCP gathers completes the migration.

For constant velocity, it can be shown that the traveltime for an equivalent offset location is indeed hyperbolic. The total traveltime may be expressed as

$$t = t_S + t_r = t_e(V_P) + t_e(V_S). \tag{2.14}$$

Through the use of Pythagoras' Theorem, this expression may be expanded to give

$$t = t_e(V_P) + t_e(V_S) = \left(\frac{h_e^2 + Z_0^2}{V_P^2}\right)^{1/2} + \left(\frac{h_e^2 + Z_0^2}{V_S^2}\right)^{1/2}. \tag{2.15}$$

Factoring the equation (2.15) reveals the espression

$$t = \left(\frac{1}{V_P} + \frac{1}{V_S}\right)\left(h_e^2 + Z_0^2\right)^{1/2}, \tag{2.16}$$

that is hyperbolic in h_e- t space.
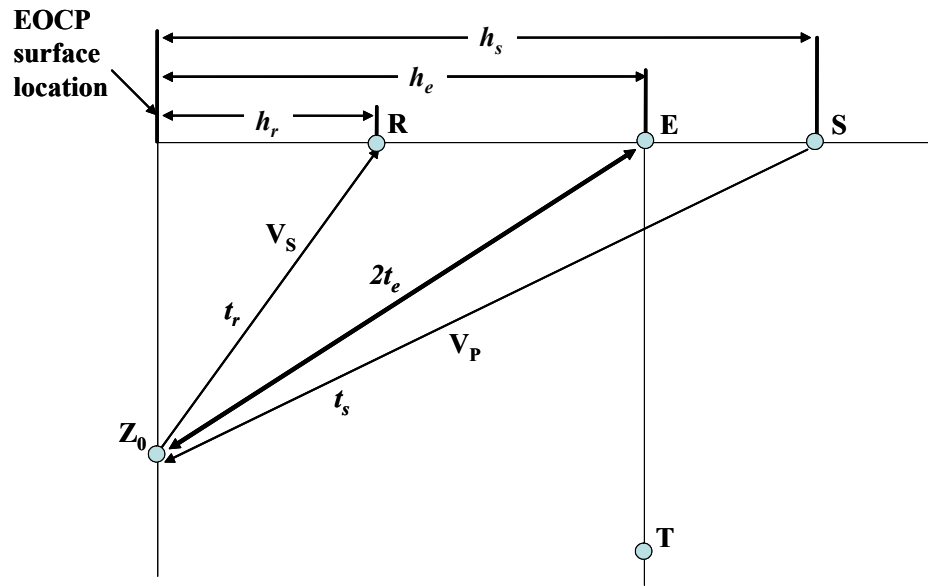
Fig. 2.5. The position and traveltimes associated with an EOCP.

2.3.3 Prow Effect

The energy from a 2D constant amplitude horizontal reflection event forms a hyperbolic cylinder within the 3D prestack volume (*x, h, t*) as shown in Figure 2.6a. A CMP gather is a vertical plane at a particular surface location, (*x=x₀, h, t*), that intersects the cylinder and contains energy along a hyperbolic curve as shown in Figure 2.6b. An EO gather is also a plane that intersects the cylinder at surface location, (*x=x₀ ,h=h_e, t*). All energy from the hyperbolic cylinder, within the migration aperture, is mapped into the gather without time shifting. Hyperbolic CMP data, zero-offset data, and all other data in between are summed into the gather as illustrated in Figure 2.6c. Horizontal reflection energy thus produces a band of specular energy bounded by the hyperbolic data near the EO plane and the horizontal zero-offset data. The energy located between these two events destructively interferes for band-limited seismic wavelets, leaving only the zero-offset and hyperbolic events which form a prow shape (bow of a yacht), as demonstrated in Figure 2.6d (Bancroft and Geiger, 1997).

To reduce the contribution of energy from zero-offset data, input samples are multiplied by a weighting factor, *w*, which is given by (Wang, 1997)

$$w = \frac{h}{h_e} \tag{2.17}$$

prior to being mapped to the given CSP gather.
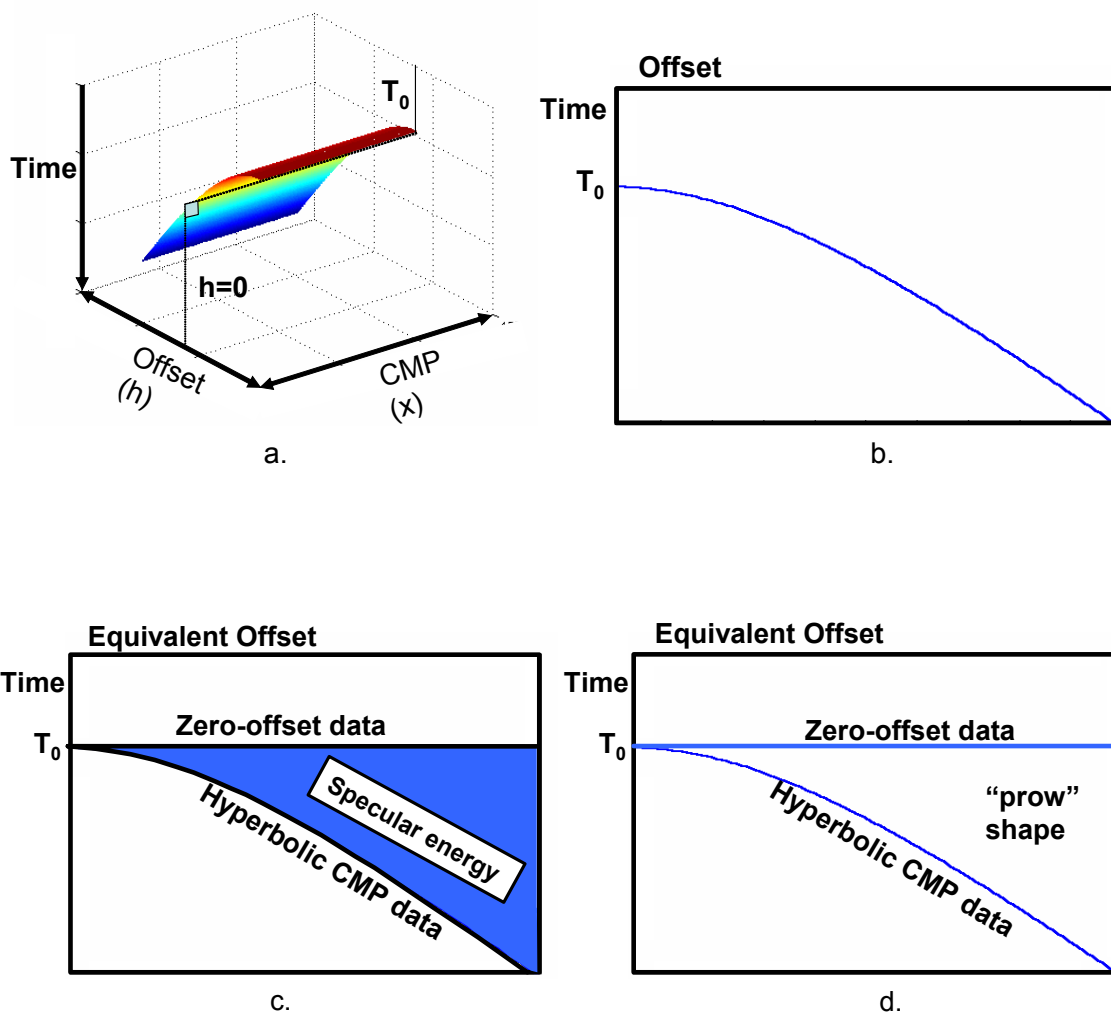
Fig. 2.6. Energy distribution for a horizontal reflector at time T_0 displayed in a) as a surface in a prestack volume *(x, h, t)*, b) a hyperbolic curve in a CMP gather before NMO, c) an EO gather with a zone of destructive interference shown in blue, and d) with constructive interference showing horizontal and hyperbolic distributions of energy to form a "prow" (Bancroft, 1997).

An AGC'ed EO gather with and without the application of the "Prow" effect filter are shown in Figure 2.7. The filter has effectively enhanced the overall S/N ratio of the gather. The hyperbolic events are better imaged and some events are illuminated that were originally invisible on the unfiltered section, as demonstrated in Figure 2.7 (a and b).
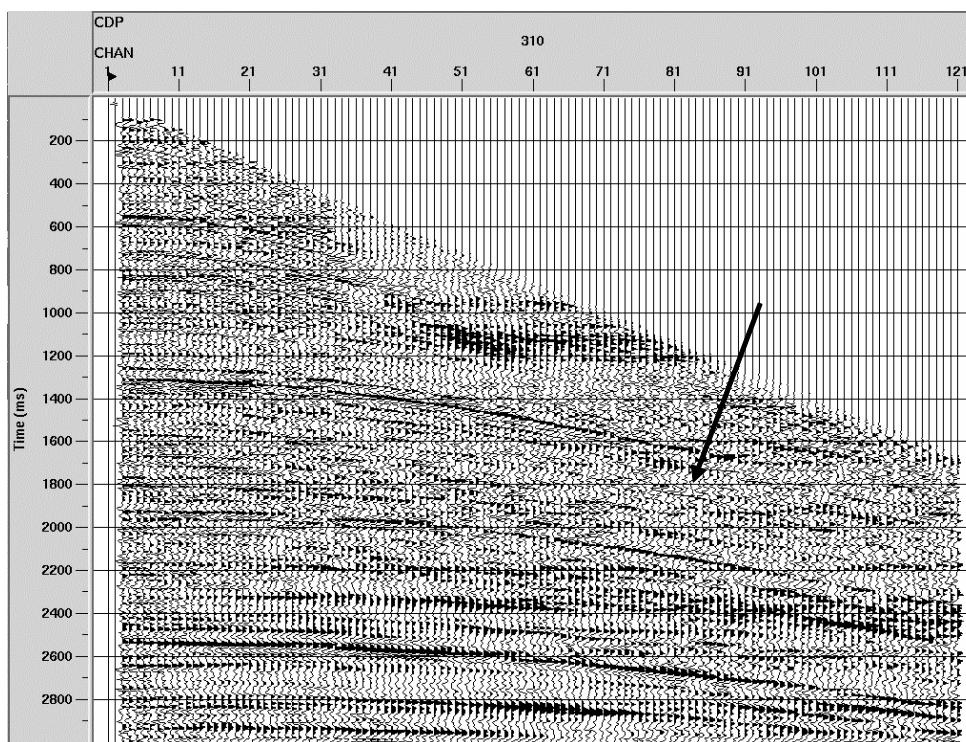
Fig. 2.7. a) EO gather of Alba data with AGC applied and no 'prow effect' filter.
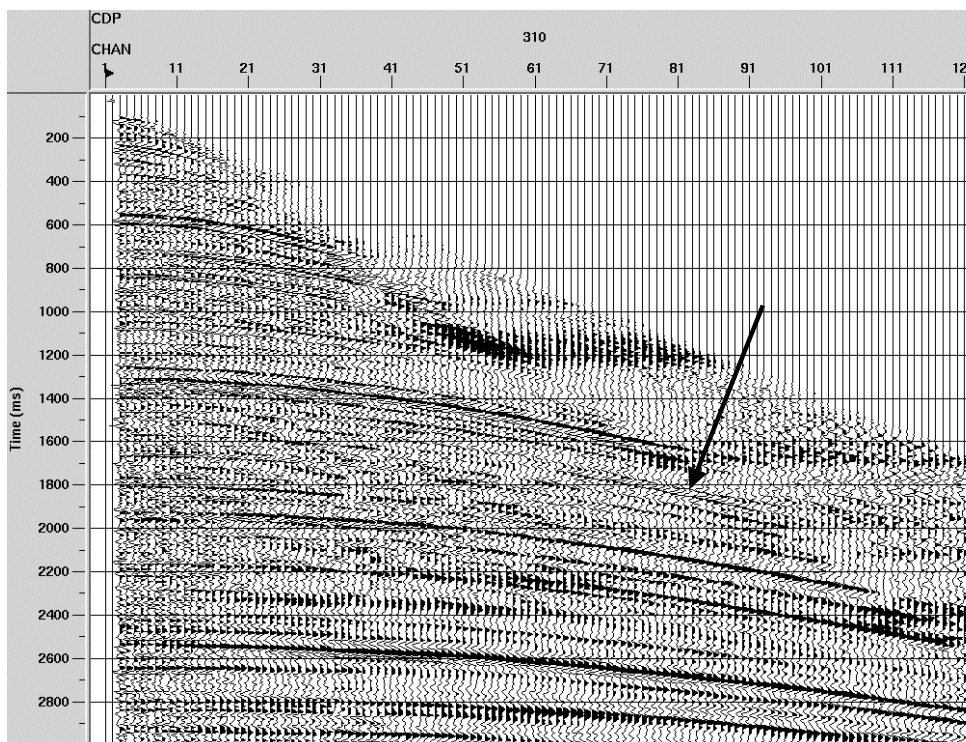
Fig. 2.7. b). Alba EO gather with 'prow effect' filter. Notice the improvement in event coherency and continuity. Arrow points to event that is not easily identified in a).

2.4 Review of AVO analysis

Reflection and transmission coefficients vary with angle of incidence. This principle is the basis for amplitude variation with offset (AVO) analysis (Castagna and Backus, 1993). Consider the partitioning of energy where two semi-infinite isotropic homogeneous bodies are in welded contact at a plane interface, as shown in Figure 2.8. The angles for the incident, reflected, and transmitted rays at the interface are related by Snell's law, where the ray parameter, P, is given by

$$p = \frac{\sin \theta_1}{V_{P1}} = \frac{\sin \theta_2}{V_{P2}} = \frac{\sin \phi_1}{V_{S1}} = \frac{\sin \phi_2}{V_{S2}}, \tag{2.18}$$

where p is the ray parameter , V_{P1} is the P-P wave velocity in medium 1, V_{P2} is the P-P wave velocity in medium 2, V_{S1} is the S-wave velocity in medium 1, V_{S2} is the S-wave velocity in medium 2, θ_1 is the incident P-P wave angle, θ_2 is the transmitted P-P wave angle, ϕ_1 is the reflected S-wave angle, and ϕ_2 is the transmitted S-wave angle.
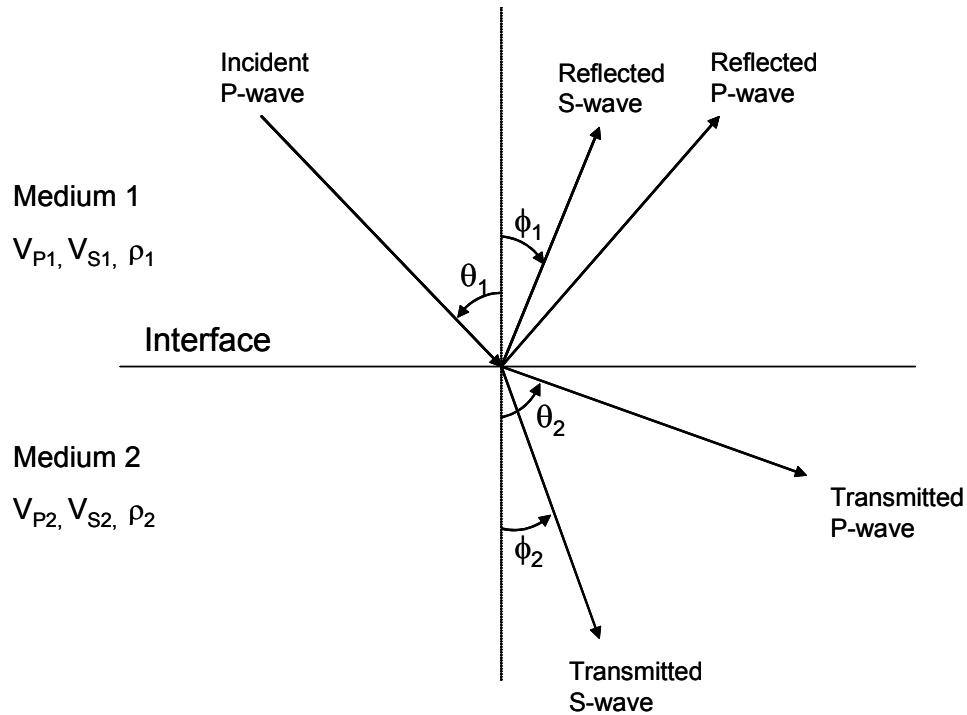
Fig. 2.8. Reflection and transmission at an interface between two infinite elastic half-spaces for an incident P-P wave (Castagna and Backus, 1993).

Knott (1899) and Zoeppritz (1919) solved for the amplitude of the reflection and transmission coefficients at a reflecting interface as a function of incident angle and the elastic properties of the media. The equations are highly complex and non-linear to the point where they are physically non-intuitive. Aki and Richards (1980) re-organized the Zoeppritz equations into a more easily solved matrix form

$$Q = P^{-1}R,$$
(2.19)

where $Q, P,$ and R are given in Appendix A.

Koefoed (1955) was the first to surmise that V_P/V_S variations could be predicted through AVO analysis, and established the following empirical rules:

"a) When the underlying medium has the greater longitudinal [P-P wave] velocity and other relevant properties of the two strata are equal to each other, an increase of Poisson's ratio for the underlying medium causes an increase of the reflection coefficient at the larger angles of incidence.

"b) When, in the above case, Poisson's ratio for the incident medium is increased, the reflection coefficient at the larger angles of incidence is thereby decreased.

"c) When, in the above case, Poisson's ratios for both media are increased and kept equal to each other, the reflection coefficient at the larger angles of incidence is thereby increased.

"d) The effect mentioned in (a) becomes more pronounced as the velocity contrast becomes smaller.

"e) Interchange of the incident and the underlying medium affects the shape of the curves only slightly, at least up to the values of the angle of incidence of about 30 degrees."

Embodied in these rules is the perception that Poisson's ratio is the elastic property most directly related to angle-dependent reflectivity. Poisson's ratio, σ, is related to V_P/V_S by

$$\sigma = \frac{\frac{1}{2}\left(\frac{V_P}{V_S}\right)^2 - 1}{\left(\frac{V_P}{V_S}\right)^2 - 1}. \qquad (2.20)$$

Many have since linearized the Zoeppritz equations (Bortfeld (1961), Richards and Frazier (1976), and Aki and Richards (1980)), by assuming relatively small changes in

elastic Earth parameters across an interface. Aki and Richards (1980) expresses the P-P wave reflection amplitude, $R(\theta)$, as

$$R(\theta) \approx \frac{1}{2}(1 - 4\frac{V_S^2}{V_P^2}\sin^2\theta)\frac{\Delta\rho}{\rho} + \frac{\sec^2\theta}{2}\frac{\Delta V_P}{V_P} - \frac{4V_S^2}{V_P^2}\sin^2\theta\frac{\Delta V_S}{V_S} \qquad (2.21)$$

where

$$\begin{aligned} \Delta V_P &= (V_{P2} - V_{P1}), \\ V_P &= (V_{P2} + V_{P1})/2, \end{aligned} \qquad (2.22)$$

$$\begin{aligned} \Delta V_S &= (V_{S2} - V_{S1}), \\ V_S &= (V_{S2} + V_{S1})/2, \end{aligned} \qquad (2.23)$$

$$\Delta\rho = (\rho_2 - \rho_1), \qquad (2.24)$$

and

$$\rho = (\rho_2 + \rho_1)/2,$$

where the incident and reflected waves are in medium 1, and the transmitted wave is in medium 2. The angle θ is the average of the incident and transmitted angles,

$$\theta = (\theta_2 + \theta_1)/2, \qquad (2.25)$$

where θ_1 and θ_2 are related by Snell's law,

$$p = \frac{\sin\theta_1}{V_1} = \frac{\sin\theta_2}{V_2}. \qquad (2.26)$$

Motivated by the perception that Poisson's ratio is the key elastic property related to offset dependent reflectivity, Shuey (1985) modified equation (2.21) by eliminating the properties V_S, and ΔV_S in favor of σ and $\Delta\sigma$. The latter are defined by

$$\Delta\sigma = \sigma_2 - \sigma_1 \qquad (2.27)$$

and

$$\sigma = (\sigma_2 + \sigma_1)/2. \tag{2.28}$$

The substitution is affected by the equation

$$V_S^2 = V_P^2 \frac{1 - 2\sigma}{2(1 - \sigma)}. \tag{2.29}$$

The resulting manipulations yield

$$R(\theta) \approx R_0 + \left[A_0 R_0 + \frac{\Delta\sigma}{(1-\sigma)^2} \right] \sin^2\theta + \frac{1}{2} \frac{\Delta V_P}{V_P} \left(\tan^2\theta - \sin^2\theta \right), \tag{2.30}$$

where the normal-incidence P-P reflection coefficient, R_0, is given by

$$R_0 \approx \frac{1}{2} \left(\frac{\Delta V_P}{V_P} + \frac{\Delta\rho}{\rho} \right), \tag{2.31}$$

$$A_0 = B - 2(1 + B) \frac{1 - 2\sigma}{1 - \sigma}, \tag{2.32}$$

and

$$B = \frac{\dfrac{\Delta V_P}{V_P}}{\dfrac{\Delta V_P}{V_P} + \dfrac{\Delta\rho}{\rho}}. \tag{2.33}$$

The coefficients (R_0, A_0, and B) are fundamental to various weighted stacking procedures. Given a NMO corrected prestack volume, these "weighted stacks", also termed "Geostacks" (Smith and Gidlow, 1987), form AVO attribute traces versus time. For each time sample on a gather, the local incidence angle is calculated. Regression analysis is then performed to solve for the coefficients of an equation of the kind:

$$R(\theta) \approx A + B \sin^2\theta + C \sin^2\theta \tan^2\theta \tag{2.34}$$

where *A* is the "intercept" or "zero-offset" stack, *B* is the "slope" or "gradient", and *C* is termed "curvature" and becomes significant at far offsets.

Hilterman (1989) derived the following intuitive approximation

$$R(\theta) \approx R_0 \cos^2 \theta + 2.25\Delta\sigma \sin^2 \theta. \tag{2.35}$$

At small angles of incidence, R_0 dominates the reflection coefficient, whereas the contrast in Poisson's ratio becomes most significant at larger angles. It follows that we can consider a near-offset stack as imaging P-P wave contrasts while the far stack images contrasts in Poisson's ratio.

2.4.1 Application of AVO

The most promising application of AVO analysis is the detection of gas sands. The characteristically low V_P/V_S ratio of gas sands should allow their differentiation from other low impedance layers such as coals or brine sands (Castagna and Backus, 1993). AVO analysis is generally performed on CMP gathers. However, EO gathers contain similar AVO information to CMP gathers for horizontal interfaces. The EO gathers can also be used to obtain AVO information from dipping reflectors (Sun, 2003).

Rutherford and Williams (1989) define three main classes of gas-sand AVO anomalies, as shown in Figure 2.11. Class 1 anomalies occur when the normal incidence P-P wave reflection is strongly positive, and demonstrates a strong amplitude decrease with increasing angle of incidence. A phase change at large offsets is possible. Class 3

anomalies are characterized by strongly negative zero-incidence reflection coefficients that get increasingly negative with increasing offset. A large percentage change in AVO is the signature of Class 2 anomalies. If the normal incidence reflection coefficient is positive, a phase reversal occurs at near to medium offsets. Due to their low impedance contrast, Class 2 anomalies can be quite difficult to image. The enhanced detection of these events is a chief focus of this research.

The same degree of reflection coefficient variation with offset is not seen in P-SV reflections. In this study, only an arbitrary P-SV wave reflection coefficient curve is used. As the reflection coefficient for all P-SV waves approach zero at normal incidence, a typical P-SV response is computed using the CREWES Zoeppritz Explorer program and is shown in Figure 2.10.
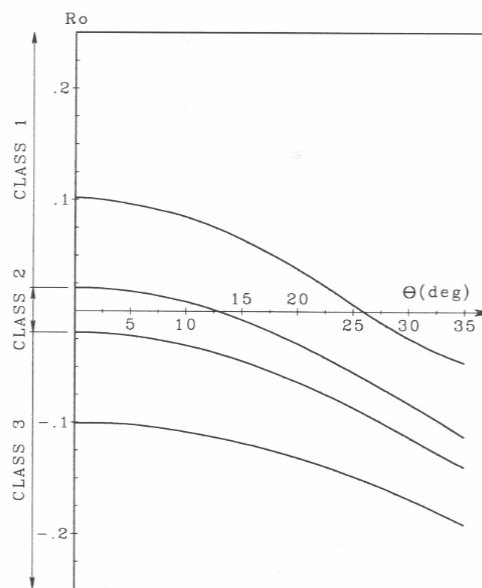
Fig. 2.9. Zoeppritz P-P wave reflection coefficients for a shale over gas sand interface for a range of R_P values. The Poisson's ratio and density were assumed to be .38 and 2.4 gm/cc for shale and 0.15 and 2.0 gm/cc for gas sand (from Rutherford and Williams, 1989).
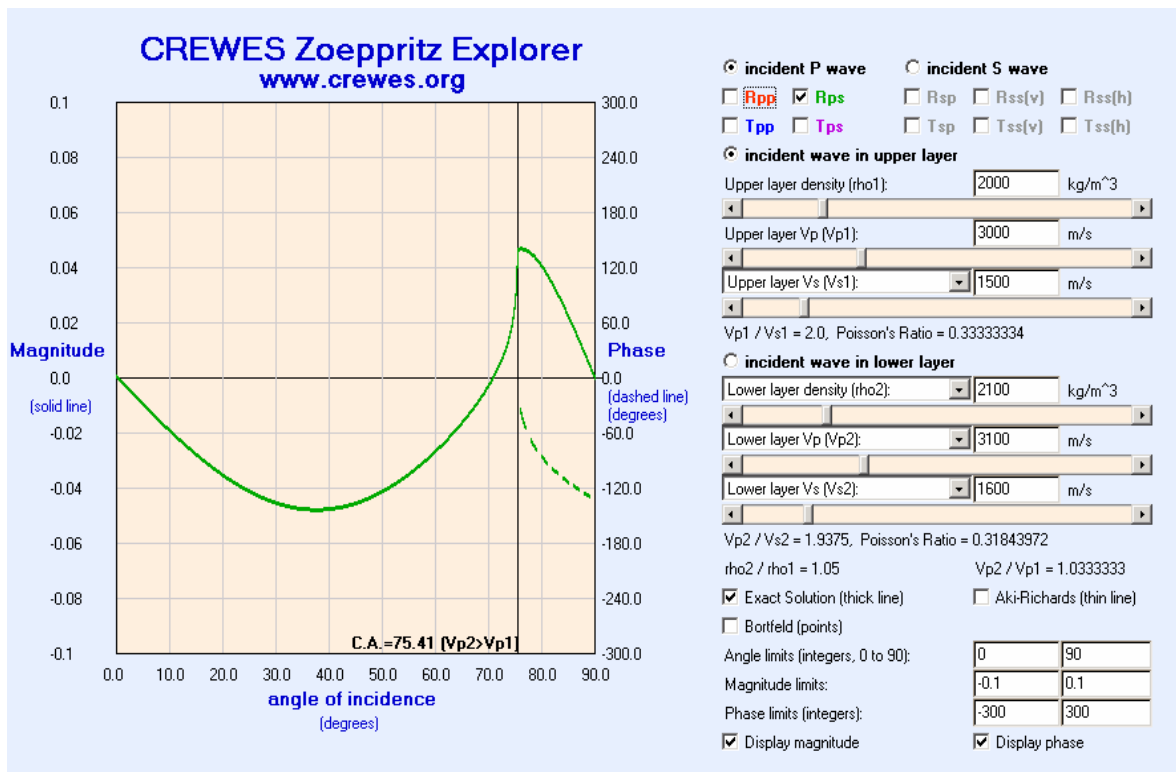
Fig. 2.10. Zoeppritz P-SV wave reflection coefficient curve for an arbitrary interface.

2.5 The matched filter

Given a particular statistical measure of signal to noise, the "matched filter" is the ideal linear filter for maximizing the S/N ratio of a signal amongst random white noise (Robinson & Treitel, 1980). Assuming a known input signal in random white noise, the matched filter is designed to maximize the signal-to-noise ratio (SNR). The following is a summary of the matched filter work of Robinson and Treitel (1980).

Suppose that the signal is the known wavelet, $(b_0,\ b_1,\ ...,b_n)$. Consider the following two situations for the received data, x_t. First, x_t could be a combination of signal and noise, u_t, as in

$$x_t = b_t + u_t \,, \tag{2.36}$$

and second, the signal may not be present, thus yielding the noisy trace

$$x_t = u_t \,. \tag{2.37}$$

The received data are fed into filter, a_t, giving the output, y_t, as

$$
\begin{aligned}
y_t &= x_t * a_t \\
y_t &= (b_t * a_t) + (u_t * a_t) \\
y_t &= c_t + v_t
\end{aligned}
\tag{2.38}
$$

where c_t and v_t are the filter responses of the pure signal and pure noise, respectively. Consider now that the filter, $(a_0, a_1, ..., a_n)$, has a length that is fixed to be equal to the length of the signal. Convolution of the filter with the received trace yields the output, y_t, as shown by

$$y_t = x_t * a_t = a_0 x_t + a_1 x_{t-1} + ... + a_n x_{t-n} \tag{2.39}$$

We need to decide, for a particular time, $t=t_0$, whether the filtered data consists of signal plus noise, or just noise. We would like to construct the filter such that the output, y_t, is greater when the signal is present in x_t, than when it is absent. This may be accomplished by making the instantaneous power in the filter output containing the signal at time t_0 as large as possible relative to the average power in the filtered noise.

Robinson and Treitel define a SNR at the filter output, μ, as

$$\mu = \frac{(\textit{Value of filtered signal at time}\,t_0)^2}{\textit{Average power of filtered noise at time}\,t_0} \,.$$

Convolution of the (N+1)-length signal, $(b_0, b_1, ..., b_n)$ with the (N+1)-length filter, $(a_0, a_1, ..., a_n)$, yields the (2N+1)-length output, $(c_0, c_1, ..., c_n, ..., c_{2n})$, where c_n is the central value of the output series. If we choose $t_0=n$, then μ becomes

$$\mu = \frac{c_n^2}{E\{v_n^2\}} = \frac{(a_0 b_n + a_1 b_{n-1} + ... + a_n b_0)^2}{E\{v_n^2\}} \qquad (2.40)$$

where $E\{v_n^2\}$ is the average value of the noise output at the instant $t=n$. Assuming that the noise is stationary and white, and through the use of Cauchy's inequality, μ is maximized when the filter, a_t, is given by (Robinson and Treitel, 1980)

$$(a_0, a_1, ..., a_n) = k(b_n, b_{n-1}, ..., b_0) \qquad (2.41)$$

where k is an arbitrary constant, which we choose to be unity for convenience. Such a filter, a_t, is termed the *matched filter* for its ability to detect signal in white noise. Notice that the memory function of the matched filter is simply a scaled version of the time-reversed signal. The matched filter convolves a_t with x_t, which is equivalent to crosscorrelating the known wavelet, b_t, with x_t.

For example, consider a 1-dimensional scenario where a minimum phase wavelet (Figure 2.11) is added to random white noise, such that the S/N ratio varies from 0.2 to 2, as given in Figure 2.12. If the wavelet is known, crosscorrelation of the wavelet with the traces in Figure 2.12 yield the results found in Figure 2.13. (Figures 2.11-13 were created by Dr. J.C. Bancroft)
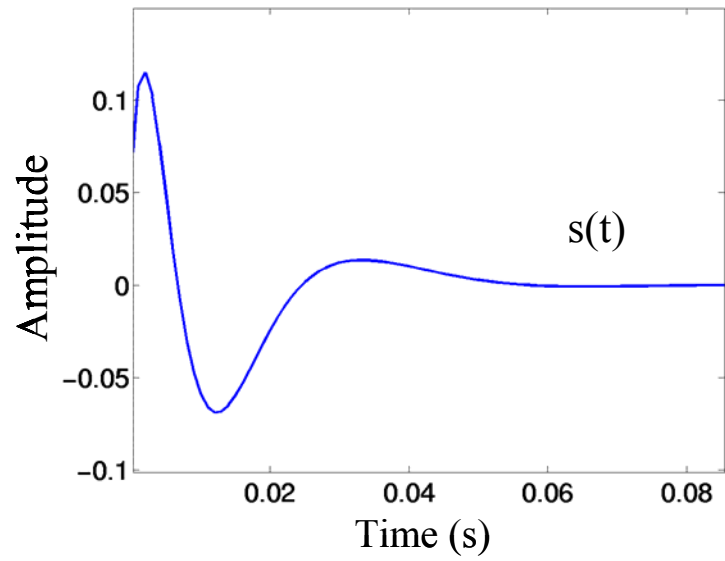
Fig. 2.11. Example minimum phase wavelet.
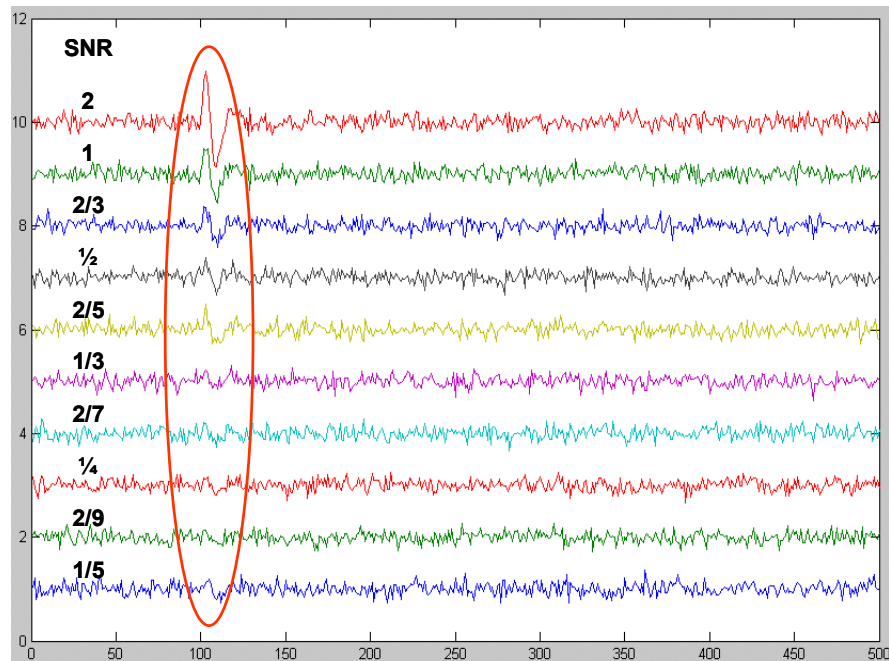
Fig. 2.12. Traces consisting of a minimum phase wavelet buried in white noise. The wavelet begins at approximately sample 100 on each trace. The S/N ratio of the traces range from 0.2 to 2 (Bancroft, Matched filter monogram, 2002).
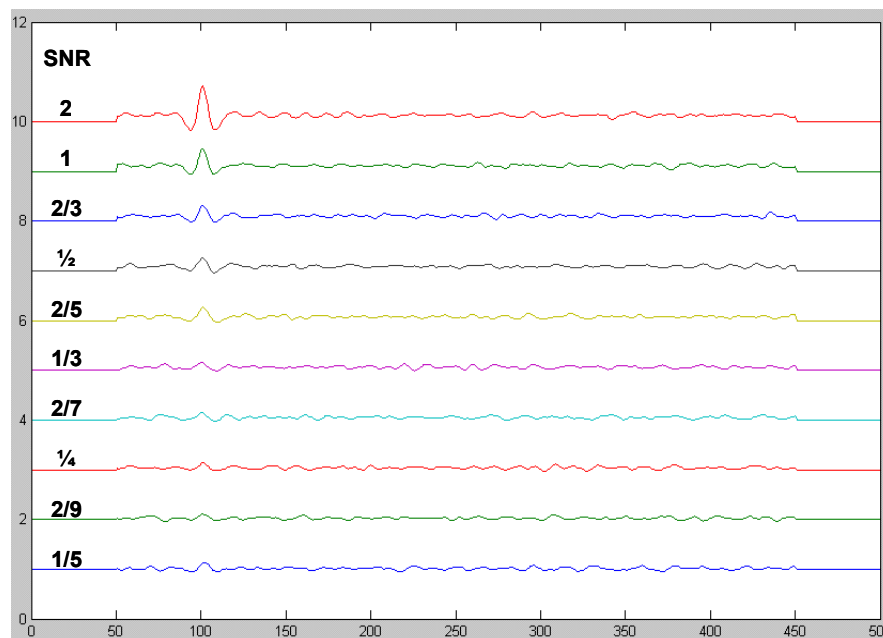
Fig. 2.13. Traces in Figure 2.12 after matched filtering with the signal (minimum phase wavelet in Fig 2.11). Notice that the embedded wavelet is now zero phase. The peak value of the wavelet corresponds to the time of maximum event detection (Bancroft, Matched filter monogram, 2002).

Notice that the embedded wavelet has changed from minimum to zero phase due to the crosscorrelation process. The peak amplitude value of the embedded zero-phase wavelet occurs at the time of maximum event detection and is a measure of the degree of event detection relative to the noise. The relative amplitude of the peaks will be proportional to the relative similarity of other wavelets with x_t.

The matched filter *guarantees* the optimum value of S/N ratio, μ, only in the presence of random, white, and stationary noise. In this analysis, the noise is assumed to be white although that assumption is not always appropriate for seismic data. Therefore, matched filtering may enhance the S/N ratio of the data, but the improvement may not be optimal. Shaping the data to whiten the noise is possible. (Robinson & Treitel, 1980).

2.6 Proposed method for matched filtered pre-stack migration

In the previous section, a simple example was used to illustrate how the matched filter could be used to maximize the S/N ratio in one-dimensional data. Through crosscorrelation of the input (signal and noise), with the known signal, the ideal SNR is achieved. A matched filter approach to event detection in prestack migration is proposed, where 'signal' is defined as a particular AVO reflection coefficient curve, and all other AVO response curves are considered 'noise'. Crosscorrelation of the prestack data with the signal illuminates reflection events whose AVO response curve matches that of the signal; other reflection energy is suppressed. Consider the 3D case of the prestack volume. According to Kirchhoff theory, seismic data is composed of signal (i.e., scatterpoint impulse responses) amongst various noise. The objective of this research is to apply a matched filter based amplitude-weighting scheme in prestack migration to maximize the imaging (i.e. SNR) of the output. Two techniques are introduced that aim to address this issue; a pre-gather method and a post-gather method. The post-gather method will be discussed first.

2.6.1 Post gather method of match filtering

Consider a CDP gather. Our model for the seismic trace, *s,* as a function of CDP location, *x*, half-source/receiver offset, *h*, and time, *t,* may be expressed as

$$s(x,h,t) = r(x,h,t) * w(x,h,t) + noise , \tag{2.42}$$

where $r(x,h,t)$ is the reflectivity, $w(x,h,t)$ is the wavelet, and * denotes convolution. Assume that the gather, located at $x=x_0$, is NMO corrected and has a stationary wavelet. We now chose time $t=t_c$ that corresponds to the peak of a wavelet with an amplitude that varies with offset. The *horizontal* seismic trace may now be expressed as

$$s(x_0,t_c,h) = s(h) = k\,r(h) + noise \tag{12.43}$$

where k is an arbitrary constant. This model is the basis for extracting "slope" and "intercept" in AVO analysis.

Consider the following diagram of the horizontal seismic trace, $s(h)$, as illustrated in Figure 2.14b. Given a known Class II type AVO signal, $r(h)$, as shown in Figure 2.14(a), noise was added to produce the output horizontal trace $s(h)$.
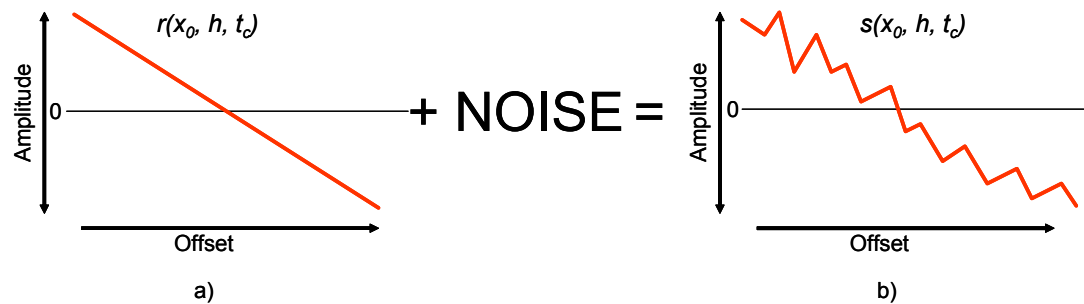
Fig. 2.14. a) Noise is added to a known signal, $r(x_0, h, t_c)$, to produce the resulting horizontal seismic trace, $s(x_0, h, t_c)$, in b).

Matched filtering is a crosscorrelation process that optimizes the SNR, and the filtered will be applied at a fixed time with varying offset. However, we are not interested in the whole crosscorrelated trace, but only in the peak value which is assumed to represent the lag of maximum signal detection. A filter, $a(h)=(a_0, a_1,..., a_n)$, is defined to be a time-reversed copy of the signal, $r(h)$, and is given as

$$a(h) = (a_0, a_1, ..., a_n) = (r_n, r_{n-1}, ..., r_0).$$ (2.44)

The filter $a(h)$ will vary with size according to the time, t, and the maximum offset of the mute pattern. Crosscorrelation of $s(h)$ and $a(h)$ yields the horizontal trace, c_k, through the relationship

$$c_k = \sum_{j=0}^{N} a_{k-j} s_j, \quad k = 0, 1, 2, ..., 2N - 1.$$ (2.45)

We chose the central value of the crosscorrelation (lag $k=n$), and assume this to represent the peak of the crosscorrelation, as in

$$cc_{k=n} = peak\ value = a_n s_0 + a_{n-1} s_1 + ... + a_0 s_n$$
$$= r_0 s_0 + r_1 s_1 + ... + r_n s_n$$ (2.46)

This equation may be expressed in matrix form as

$$cc_{k=n} = \begin{bmatrix} s_0 & s_1 & s_2 & \cdots & s_n \end{bmatrix} \begin{bmatrix} a_n \\ a_{n-1} \\ a_{n-2} \\ ... \\ a_0 \end{bmatrix}.$$ (2.47)

The above matrix representation reveals that the matched filtering process is essentially a weighted stacking procedure. A conventional stack occurs when all of the coefficients of $a(h)$ are equal to unity. However, a peak value representing maximum event detection occurs when $a(h)=r(-h)$.

The proposed matched filter method of event detection requires a user-specified filter, $a(h)$, that represents a particular AVO response that we hope to enhance. Incorporation of this weighting function will therefore tend to output greater values when the memory function of the filter matches the offset dependent reflectivity, $r(h)$, that is

buried in the noisy trace, *s(h)*. If our goal is to detect events with significant AVO behaviour, we may choose coefficients for *a(h)* that range linearly from 1 to -1. The weighted stacking process would tend to cancel events with little AVO behaviour, and enhance events that demonstrate significant AVO response. Events whose AVO response most closely matches the memory function of the filter (Class II AVO events) will be best detected.

The kinematics of the matched filtering process is illustrated in Figure 2.15. A horizontal seismic trace, $s(x=x_0, h, t= t_c)$, in a NMO corrected 3D prestack seismic volume, is matched filtered by a linear ramp memory function, and stacked to produce an output sample on a 2D section (Fig. 2.15 c).
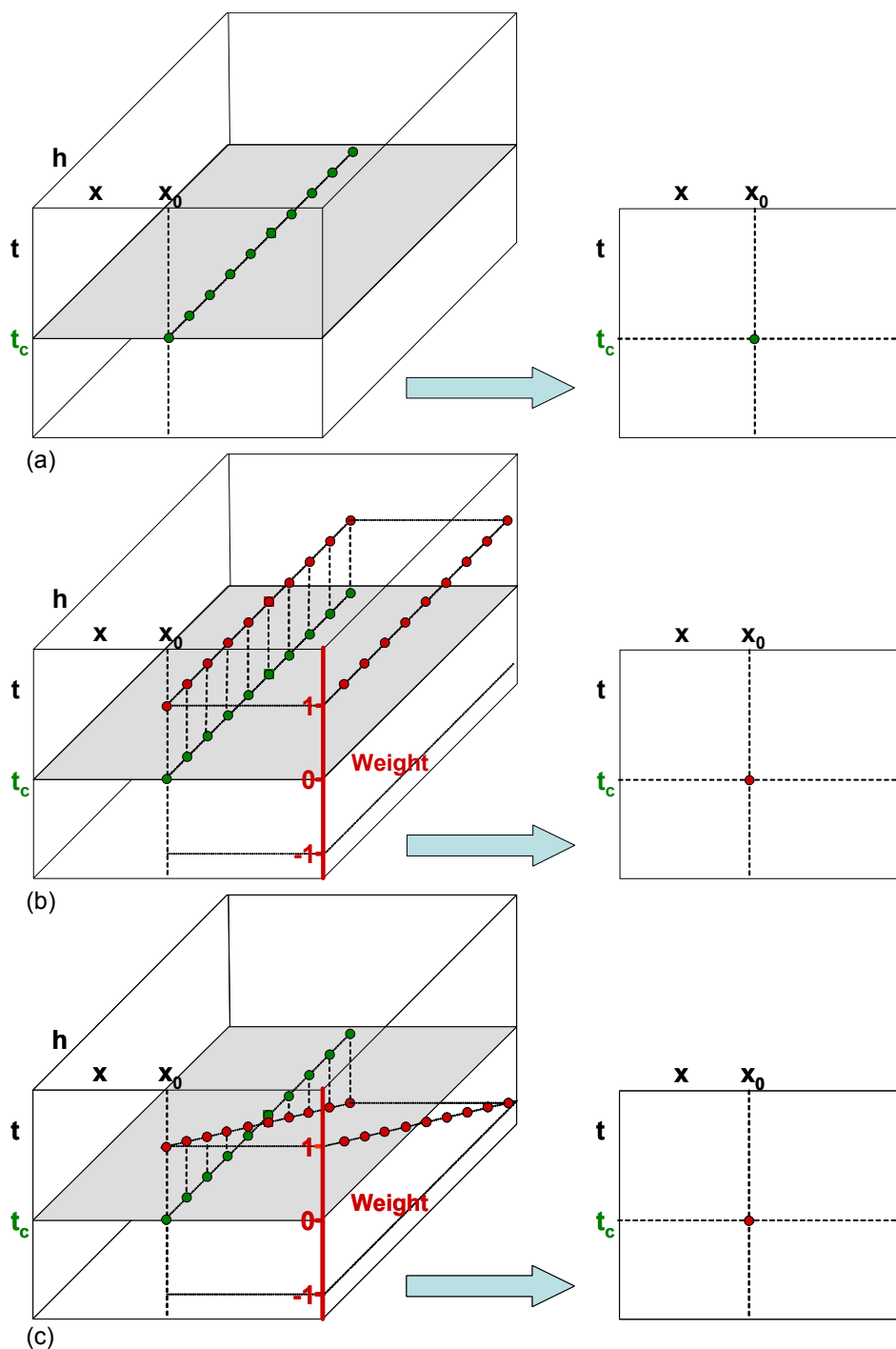
Fig. 2.15. A kinematical description of the weighted stacking procedure is shown. Note that the green dots represent the NMO corrected seismic trace, and the red dots represent the coefficients of the matched filter. A NMO corrected seismic trace is stacked and shown in a). This procedure is equivalent to weighting each sample by unity prior to stacking as shown in b). A linear ramp function is chosen for the weighting coefficients in c). This choice of filter tends to cancel events with little AVO response and enhance events with strong AVO response. Class II AVO events are particularly well detected as their AVO response closely matches the filter.

Consider an exaggerated, hypothetical NMO corrected CMP or EO gather that is shown in Figure 2.16. Random white noise has been added to the section. Event 1 represents a typical P-P wave reflection event with constant AVO response. Event 2 represents a Class II AVO reflection. The reflection coefficient curve for each event is shown in Figure 2.17; note that the reflection coefficient is assumed to be dependent on offset, not angle of incidence. Conventional stacking of this gather yields an output trace where Event 1 is well imaged but Event 2 is poorly imaged due to the amplitude polarity change at mid-offsets. The trace produced from the stacked section is shown to the right of the section in Figure 2.16. If the goal of the processing is to maximize the event detection, or imaging, of Event 2 relative to Event 1 and the noise, a matched-filter based amplitude-weighting function may be applied to discriminate Event 2 from Event 1. Let the reflection coefficient (RC) curve for Event 2 be considered as 'signal', and any other shaped RC curve be considered as 'noise' (including the curve for Event 1). According to matched filter theory, crosscorrelation of the input data (EO gather) RC curve of Event 2 yields maximum event detection of Event 2. The shape of the RC curve of Event 2 can be approximated by a linear ramp function that has a value of −1 at zero offset, and a value of 1 at maximum offset (i.e. at the edge of the mute). For each time sample, the seismic data is multiplied by a ramp function that extends from zero offset to the mute, as shown in Figure 2.18. Crosscorrelating of this ramp function with the EO gather prior to stacking will tend to reinforce the event we hope to image, and simultaneously cancel the energy of events with constant AVO response, as shown in Figure 2.19.
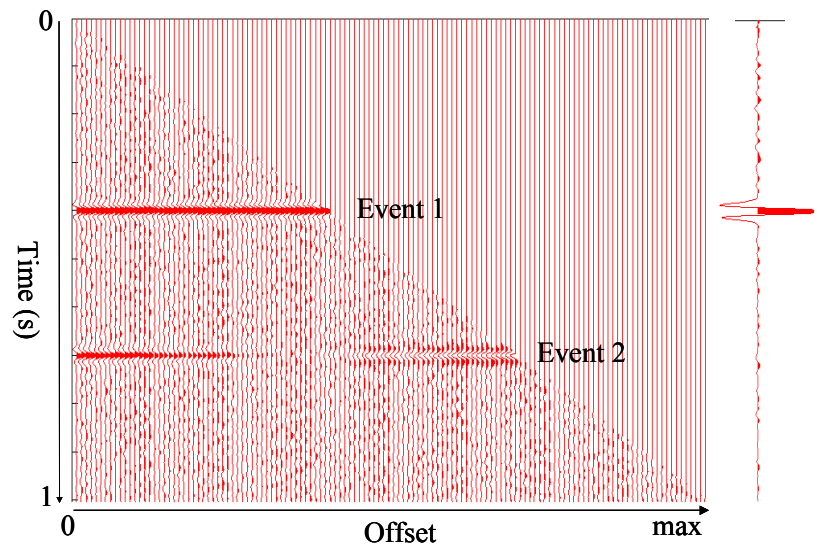
Fig. 2.16. Hypothetical NMO corrected EO gather with random white noise. Event 1 has constant AVO response and Event 2 is a class II AVO anomaly. Output trace resulting from the stacked section is shown on the right.
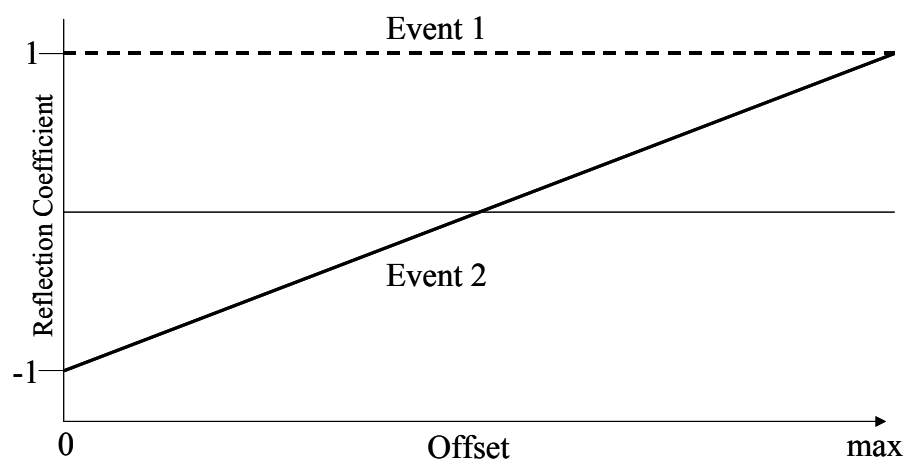
Fig. 2.17. Reflection coefficient vs. angle of incidence functions for Events 1 and 2.
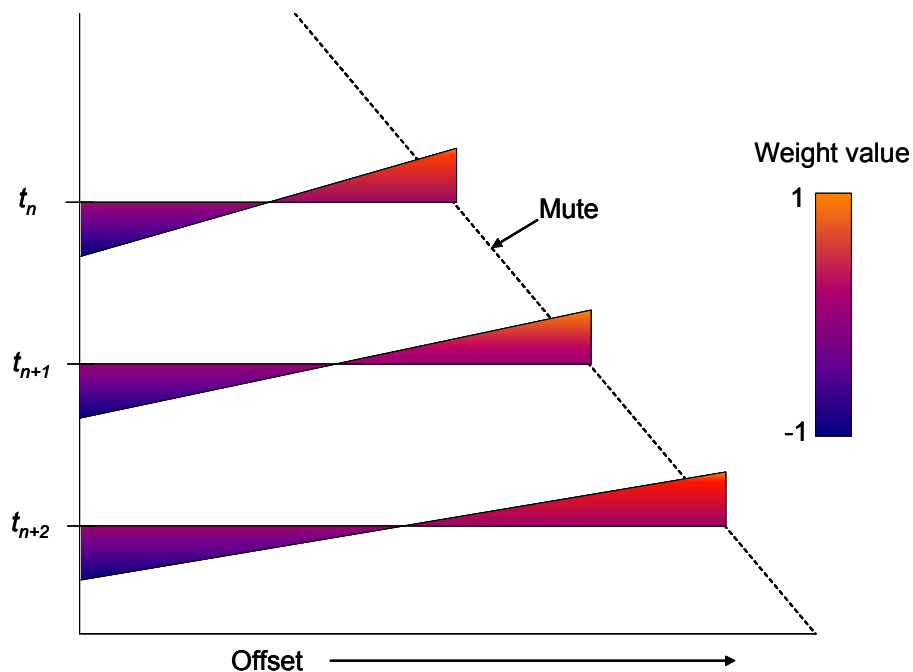
Fig. 2.18. Kinematical illustration of matched filtering an EO gather with a ramp function. The data at each time sample is multiplied by a ramp that extends from zero offset to the edge of the mute.
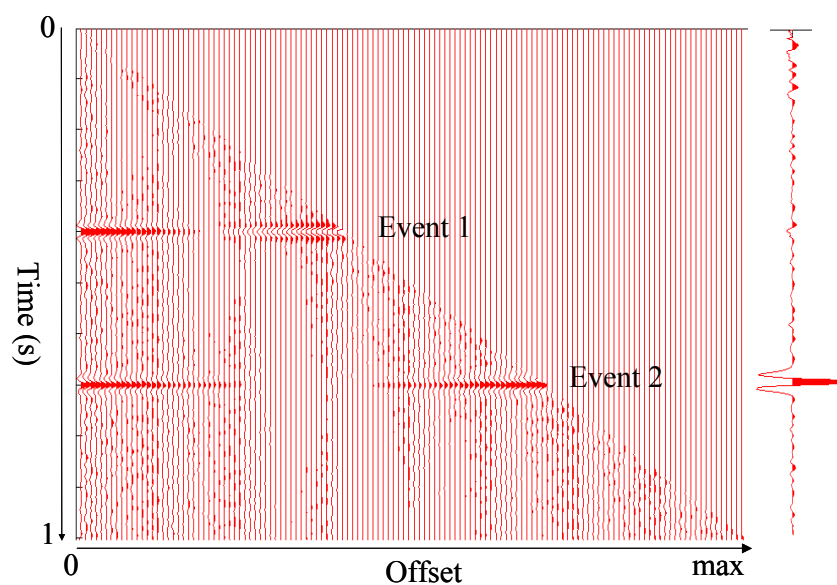
Fig. 2.19. Gather shown in Figure 2.16 after crosscorrelation with a linear ramp function (-1 to 1) that has approximated from the RC curve of Event 2. Event 1 now demonstrates a polarity reversal at mid-offsets, whereas the amplitudes of Event 2 are now all positive. The resulting stacked trace is shown to the right of the section.

Energy cancellation of conventional, constant AVO response P-P wave reflection energy is the motivation behind the application of the −1 to 1 ramp function. This "brute force" method of matched filter weighting is computationally inexpensive, robust, and has the potential to be an effective tool in the detection of AVO anomalies. It is particularly well suited for the imaging of Class II AVO anomalies, where the amplitude of a reflection event changes polarity at mid-offsets. The better the match between the Class II AVO event response with the −1 to 1 ramp function, the better the imaging of the said event.

2.6.2 A note on event polarity

Due to the nature of the above matched filtering process, it is likely that many events in the output section will have changed polarity. The output polarity of an event is largely dominated by the RC curve of the event in question and the RC curve of the 'signal' event. Other factors that may affect the output polarity of an arbitrary event include noise and residual moveout.

2.6.3 A more realistic model

The previous model assumed the following:

- Event 1 had a flat RC curve.

- The RC curve of Event 2 was equivalent to that of the filter.

- The NMO correction was perfect.

In this section, further synthetic testing is discussed where a more realistic model is used where the previous assumptions are not met.

A new constant velocity model has been constructed where the RC curves of Events 1 and 2 are shown in Figure 2.20a. The RC curves for Events 1 and 2 in this model are better approximations to those that may be encountered in real data. The RC curve of Event 1 is not flat, and Event 2 represents a more realistic Class 2 AVO anomaly that does not match the ramp function as well as that of the previous model. A perfectly NMO corrected EO gather and its stacked trace resulting from this model are shown Figure 2.21. Again, the objective is to convolve the section with the ramp function (Figure 2.20b) in order to destructively cancel Event 1 and improve the S/N of Event 2 through stacking. 'Signal' now refers to reflection amplitude curves that match the ramp function curve from zero offset to the mute. The greater the deviation of an event's RC curve with that of the ramp function, the more it is considered noise. Matched filtering of the input data with the ramp function yields the effective RC curves for Events 1 and 2 (Figure 2.20 c). The match filtered EO gather is shown in Figure 2.22.
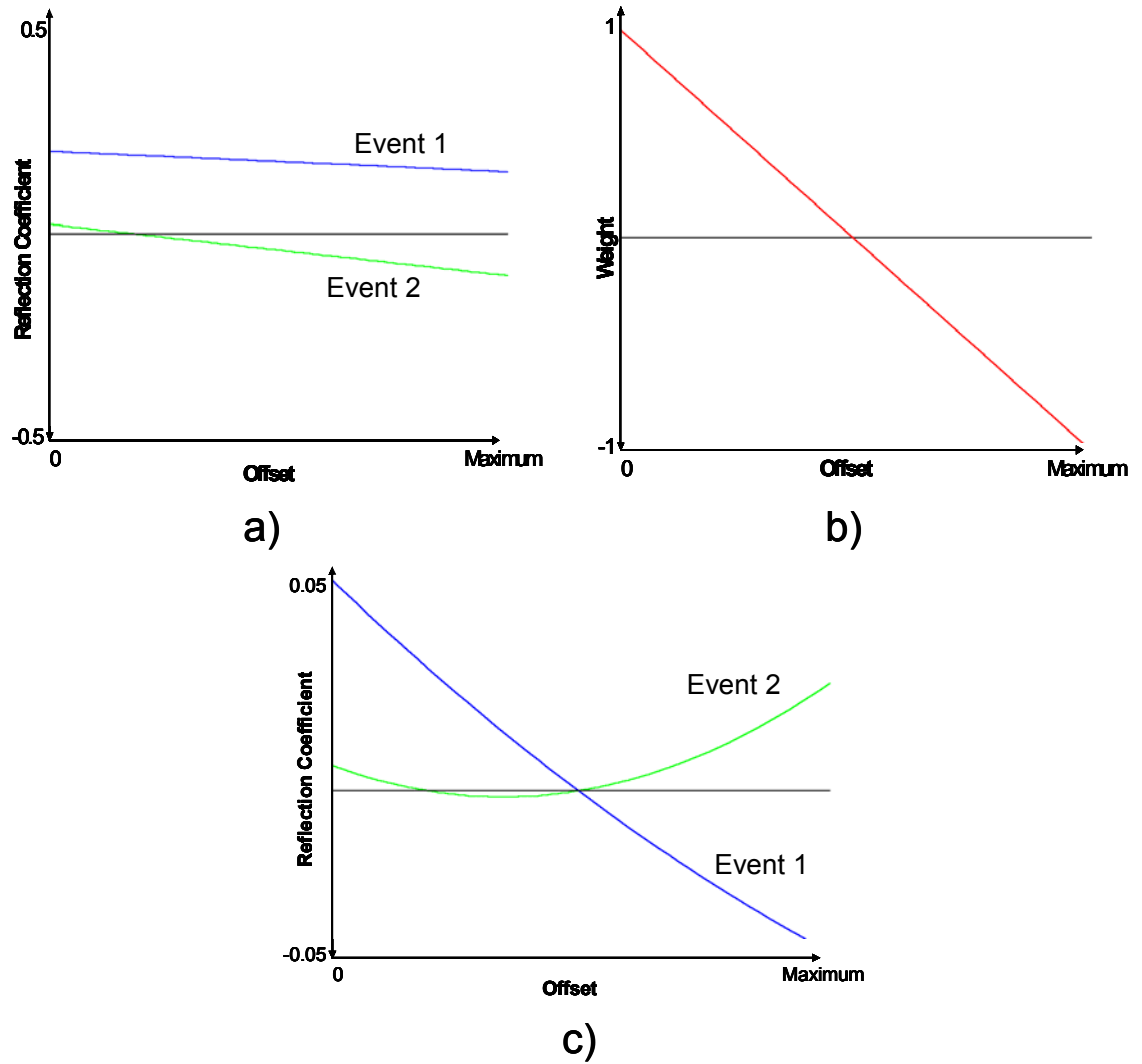
Fig. 2.20. a) Model reflection coefficient curves for Events 1 and 2. b) Linear ramp weighting function that crosses zero at mid-offset. c) Effective reflection coefficient curves of Events 1 and 2 after being multiplied by b).
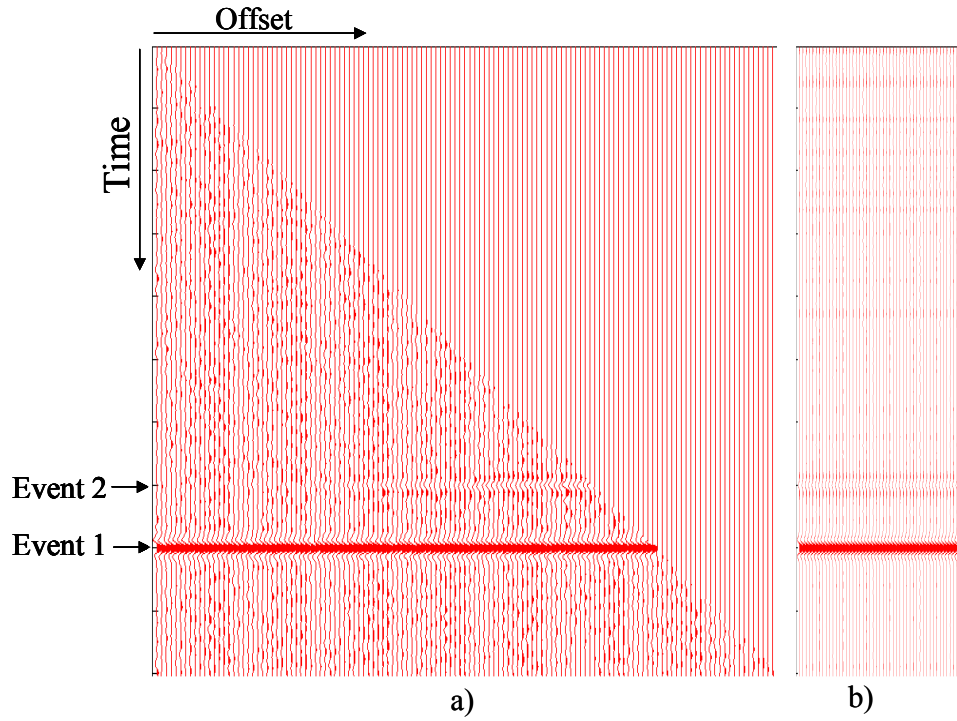
Fig. 2.21. a) Synthetic EO gather. b) Stack of (a) copied 50 times.
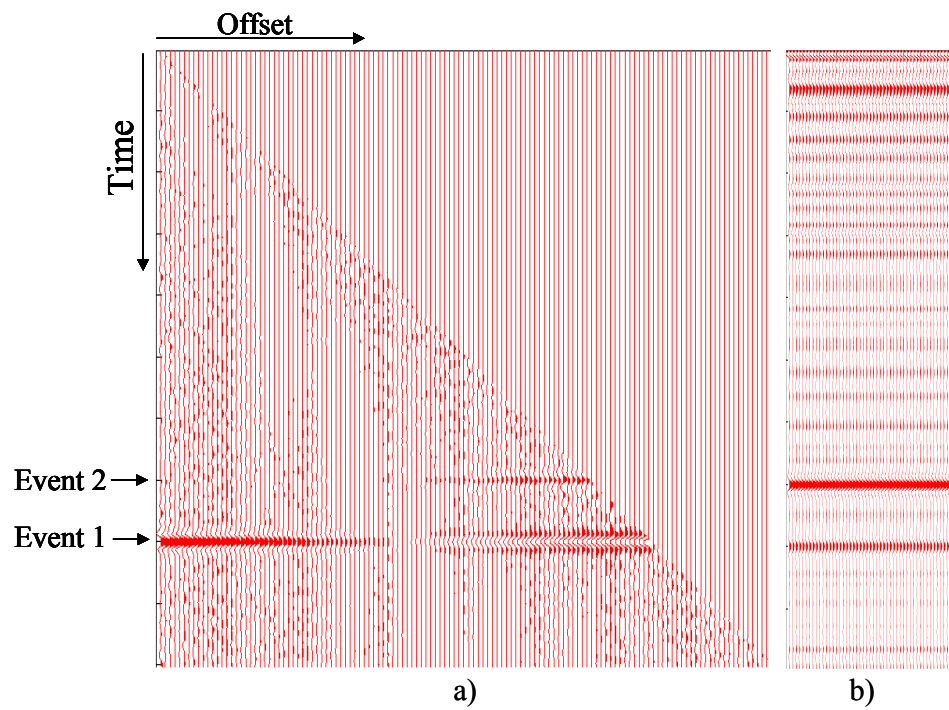
Fig. 2.22. a) Matched filtered EO gather. b) Stack of (a) copied 50 times.

Notice that the effects of matched filtering are:

1) Event 1 reflection energy has been suppressed, but not completely cancelled.

2) Event 2 is better detected than Event 1.

3) Polarity of Event 2 has reversed.

Although the energy cancellation of Event 1 and the constructive interference of Event 2 are not as complete as in the ideal scenario (Figure 2.19), the matched filter has succeeded in imaging the AVO anomaly relative to the conventional P-P wave reflection. The better the match between the RC curve of a particular AVO Event and the filter, the greater the degree of event detection.

2.7 Velocity sensitivity of Post-gather method

In the previous section, it was shown that the degree of event cancellation, or event construction, was dependent on the shape of the RC curve of the reflection event for perfectly NMO corrected events. In this section, it will be shown how the degree of event detection also depends on the accuracy of NMO correction.

Figure 2.23 demonstrates the sensitivity of the post-gather method of matched filtered event detection to velocity errors. On the left of Figure 2.23, the same synthetic stacked section is shown as in Figure 2.21. The four sections on the right have been matched filtered in the same manner as shown in Figure 2.22; however velocity errors

have been introduced. Notice that small errors in velocity result in a significant degradation of S/N of Event 2 relative to Event 1 after match filtering. These figures illustrate the need for accurate velocity estimation when applying AVO analysis. The EO method does provide these accurate velocities.
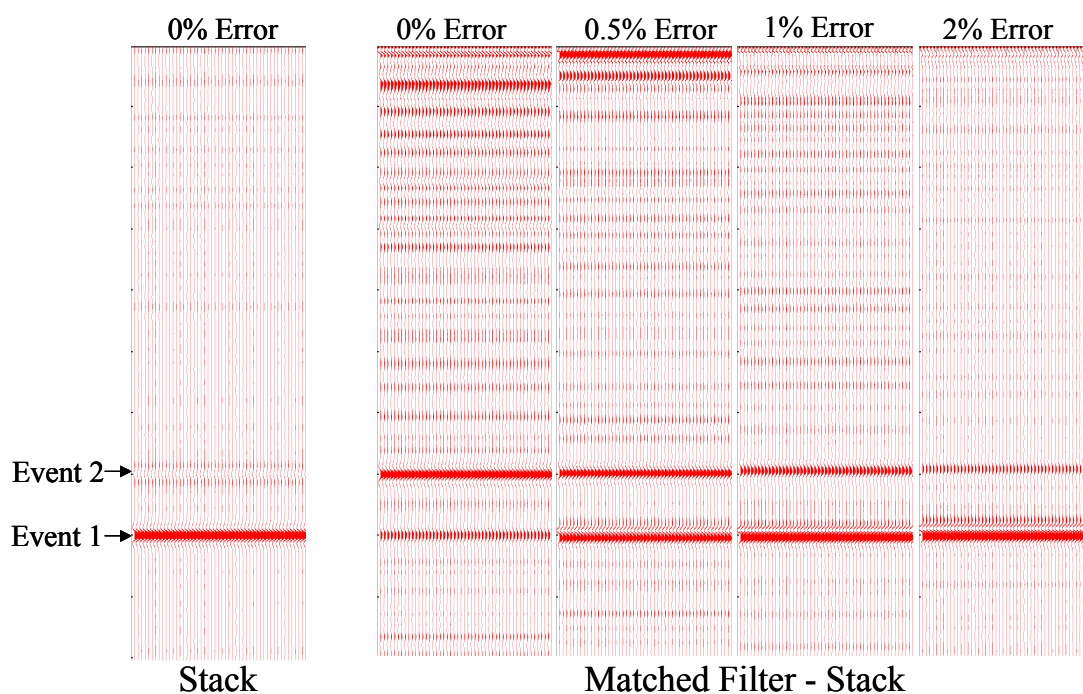
Fig. 2.23. Shown on the left is the stacked section in Figure 2.20. The four sections on the right have been matched filtered in the same manner as shown in Figure 2.21, but small velocity errors have been introduced prior to stacking.

2.8 EO method of matched filtering

We can alternatively apply a matched filter based amplitude weighting function in concert with the EO gathering process, as opposed to a CMP application. The following section describes this pre-gather method of event detection.

Consider now a 2D P-SV data seismic survey. The proposed method assumes that each scatterpoint is a dipping, elemental reflector of finite length. The first step is to choose the elastic Earth parameters of the interface that is to be imaged. A typical RC curve for a P-SV reflection is given in Figure 2.24. Recall the P-SV traveltime surface shown in Figure 2.3 and the prestack geometry shown in Figure 2.1. For an arbitrary scatterpoint, the angles made by the scatterpoint with the sources and receivers are calculated for all x and h locations above the scatterpoint. The incident angles can then be approximated with knowledge of the V_P/V_S ratio at the scatterpoint. Through knowledge of the incident angles for all x and h, and the Earth parameters of the scatterpoint to be imaged (a reflection event being an organised arrangement of scatterpoints with similar elastic properties), a Zoeppritz defined RC surface may be calculated. An example surface is shown in Figure 2.25. Each sample on the scatterpoint traveltime surface is multiplied by the appropriate reflection coefficient prior to summation as illustrated in Figure 2.26. This process is then repeated for all scatterpoints during the EO gathering process. As a result, greater weight is given to samples with greater signal content, and input samples with greater noise content are suppressed. For example, input samples on a P-SV traveltime surface from a co-located source and receiver generally do not contribute any signal and are given a weight of zero.
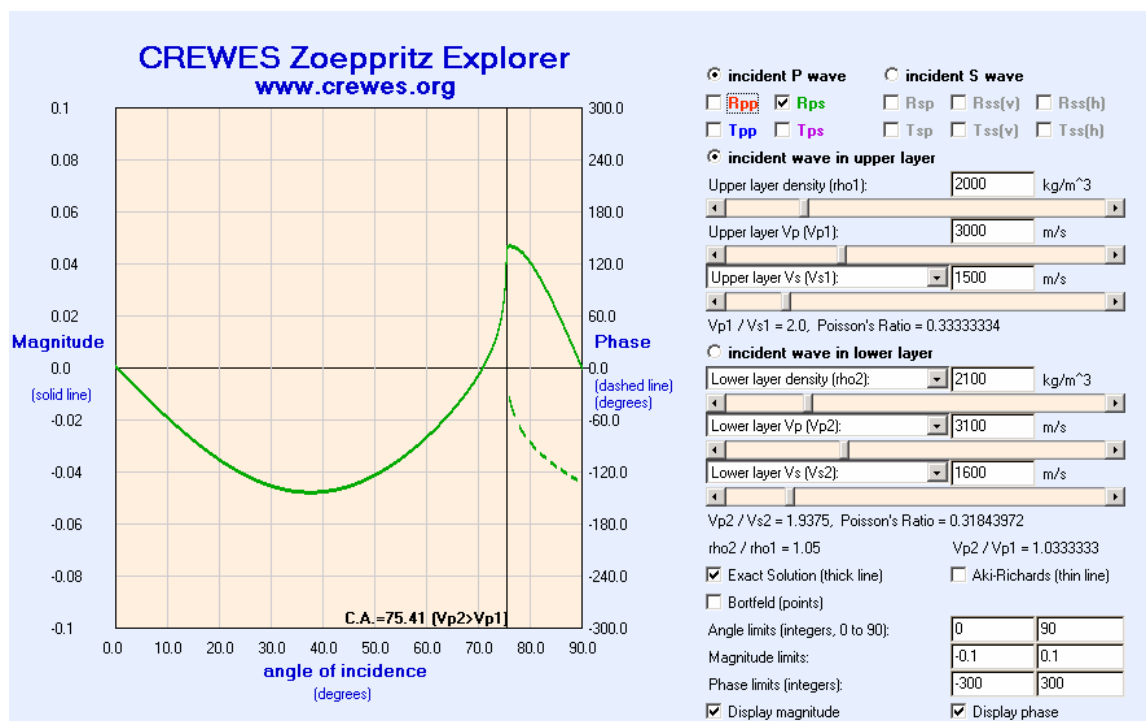
Fig. 2.24. Reflection coefficient curve for an arbitrary P-SV event.
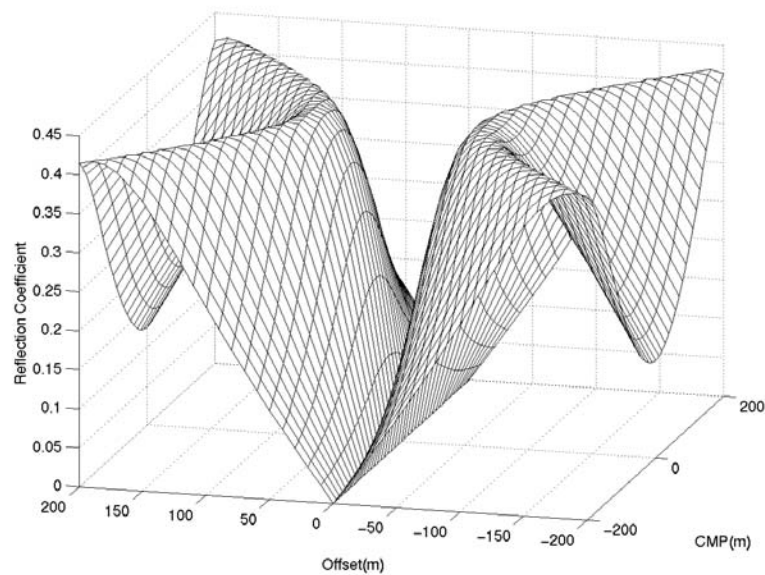
Fig. 2.25. Example P-SV reflection coefficient surface produced from a scatterpoint.
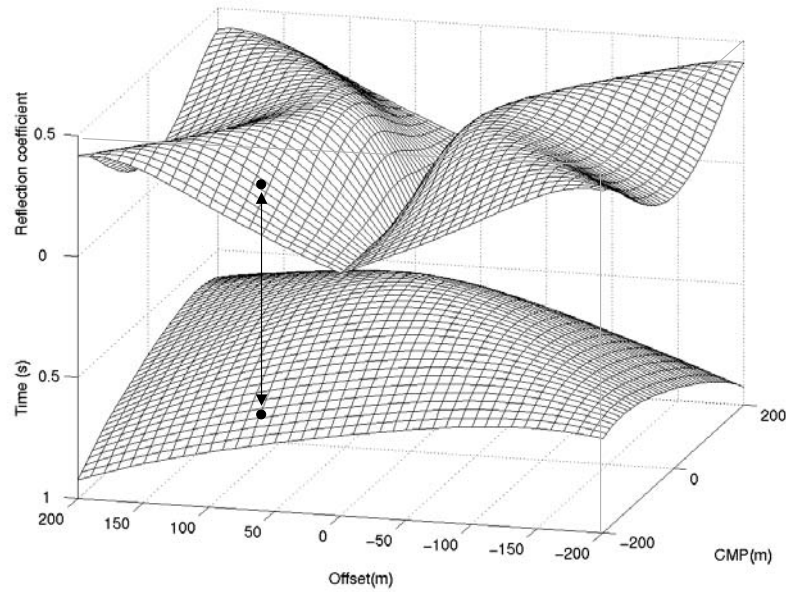
Fig. 2.26. Zoeppritz defined reflection coefficient surface plotted over a traveltime surface. Sample located at CMP(x), Offset(h) is shown to be scaled (multiplied) by reflection coefficient at CMP(x),Offset(h).

The pre-gather method of matched filter amplitude weighting is more computationally expensive due to the greater amount of data, and the necessity of calculating angles of incidence for every input sample. However, the pre-gather method may have the potential for achieving superior results.

2.9 Matched filter imaging vs. conventional AVO analysis.

Traditionally, AVO attributes are calculated from prestack data following a linearized approximation to the AVO Zoeppritz equation, e.g. Shuey (1985). Various linear combinations of the fundamental AVO attributes (intercept, *A,* and gradient, *B*) may be formed to display AVO information, e.g. gradient stacks or *A*B* stacks. The use

of a technique called Geostack (Smith and Gidlow, 1985) by Fatti *et al*. (1994) resulted in a significant discovery which is now a considered a classic example of gas sand detection using AVO analysis. The key AVO attribute in the Geostack technique is the 'fluid factor' attribute (Smith and Gidlow, 1987).

In order to perform AVO analysis properly, some *a priori* knowledge is required. First, a P-P wave velocity model is required to calculate a relationship between offset and angle of incidence. In addition, a background *Vp/Vs* ratio needs to be assumed. The EO matched filtering process also requires this *a priori* knowledge. However, the advantage that the post-gather method of matched filtering (as shown in Figure 2.18) holds over AVO attributes is that no additional information is required to detect AVO anomalies. All that is required is a user-specified curve. In this thesis, a simple ramp function was found to be highly effective in both the energy cancellation of events with no AVO response, and in the enhancement of events with significant AVO response. Class II AVO events are particularly well-imaged using the ramp function.

Another common procedure is to compare near and far stacks. This is an effective tool in the detection of AVO anomalies where the near offset response is significantly different to the far offset response. However, low impedance contrast Class II AVO events exhibit weak and similar near offset and far offset responses, although a phase change may be observed. As shown in this thesis, both post-gather and EO match filtering processes readily images these events.

2.10 Conclusions

The degree of S/N enhancement in the proposed method of matched filtered pre-stack migration is governed by the difference in AVO response between the 'signal' and 'noise' reflection events.

P-P and P-SV wave data RC curves have fundamental differences, resulting in the possibility of different applications of the matched filter. For a typical P-SV RC curve, the reflection coefficient is largest at mid-offsets, and approaches zero as the incident angle approaches zero degrees. In Chapter 3, it will be demonstrated how matched filtering of the data during migration with a general P-SV RC curve suppresses much noise in the prestack data, resulting in an image with enhanced S/N ratio.

However, the situation is different with P-P wave data. RC curves for P-P wave reflection events are relatively constant over the range of incident angles (i.e. when V_P, V_S, and ρ increase with depth). Matched filtering of the input data by a flat curve (i.e. constant RC value for all incident angles) yields no change in image enhancement. However, there are some exciting possibilities for the matched filter in the detection and imaging of Class II anomalies, as explored in Chapter 4. The matched-filtering of input data with a Class II AVO curve results in the energy cancellation of events with little AVO response, as shown in Figure 2.19.

It is important to note that the matched filtering process described in this thesis is only a tool to be used for event detection. The amplitude of an event in a matched filtered

section only describes the relative similarity between the AVO response of the interface that created the original seismic event, and the 'signal' AVO curve used in the matched filtering process. Unlike a weighted stack obtained through AVO analysis, a matched filtered section may not be inverted to obtain petrophysical properties.

The application of matched filtering to P-P and P-SV wave field data is described in the following two chapters.

Chapter 3: P-SV wave imaging using matched filters

3.1 Introduction

Up to this point, the theory of matched filters has been presented, and how they may be applied to enhance seismic imaging. This chapter concerns the application of matched filters in the imaging of converted-wave (P-SV) data. First, a test on P-SV synthetic data will be discussed followed by an application of the matched filter in the imaging of P-SV data acquired over the Blackfoot oil field in Alberta, Canada.

3.2 P-SV Synthetic test

Synthetic P-SV pre-stack data were created for a single, flat reflector model using MATLAB. The model Earth parameters were chosen to incorporate a large range of reflection coefficients, and are found in Figure 3.1.
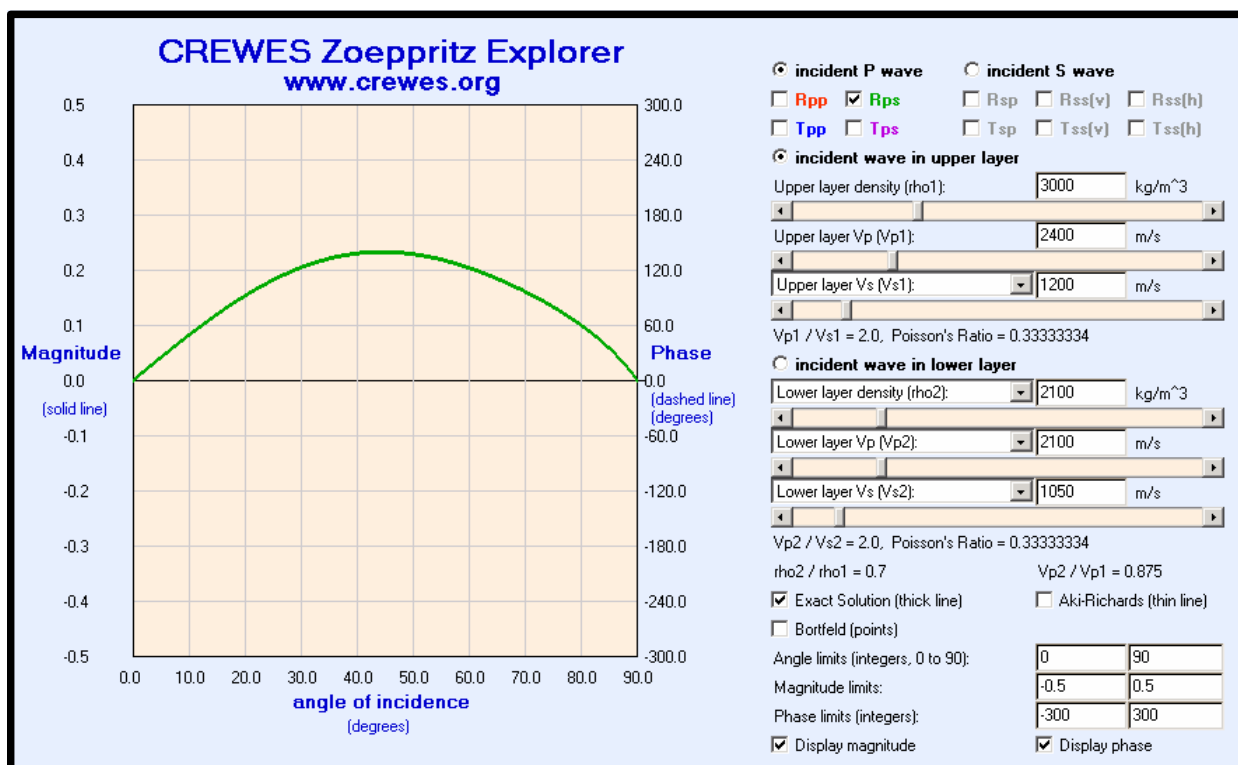
Fig. 3.1. Elastic parameters and Zoeppritz reflection coefficient curve for a single layer P-SV synthetic model.

The data were acquired in a split-spread survey with 25m shot and receiver intervals, a maximum offset of 1250m, and a 2ms sample rate was used. The reflector is located at a depth of 400m.

A 30-Hz Ricker wavelet is used as the source. Noise was added to the section such that the signal to noise ratio equals 1. The RMS value of the signal on an arbitrary pilot trace is calculated and the standard deviation of the noise is given as: noise power = (signal power) / (signal to noise ratio). For each prestack trace, a pseudo-random noise vector was calculated and added to the trace. An S/N ratio of 1 was used in calculating noise for all traces. Polarity has also been reversed for traces with negative offsets, and

the data has been scaled to compensate for geometrical spreading. An example shot record is found in Figure 3.2.
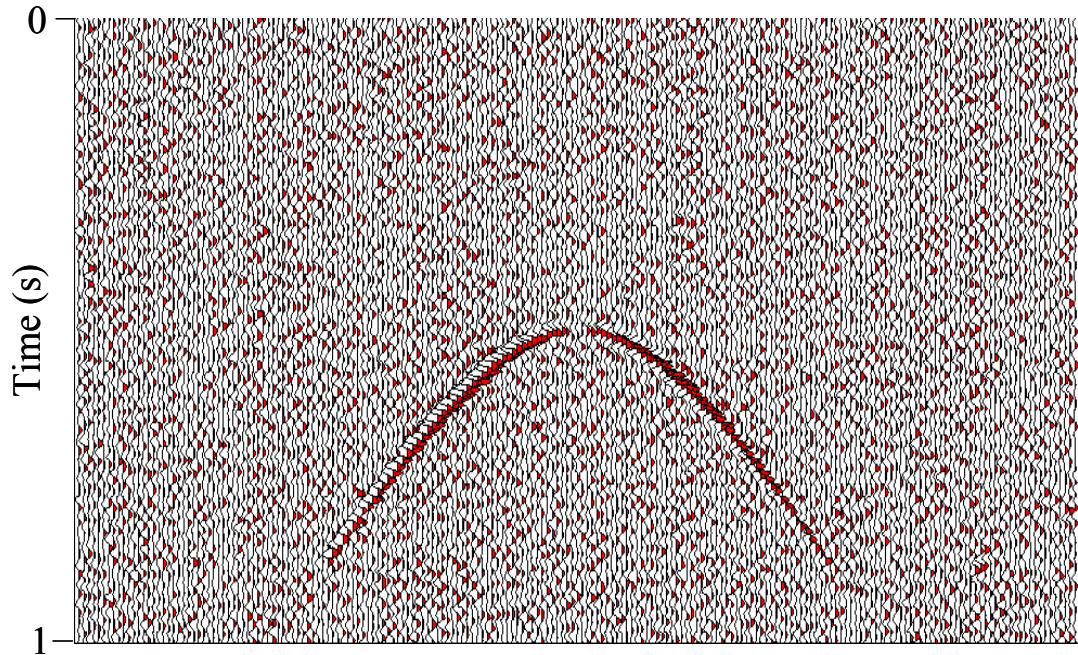
Fig. 3.2. Example P-SV wave synthetic shot record.

An equivalent offset conversion point (EOCP) gather located at x=1250m <u>without any amplitude scaling</u> is shown in Figure 3.3. Notice that the gather is very noisy, particularly at near equivalent offsets where there is little signal content. High amplitude noise is apparent along the dip-limit due to edge effects of the EOCP gathering.
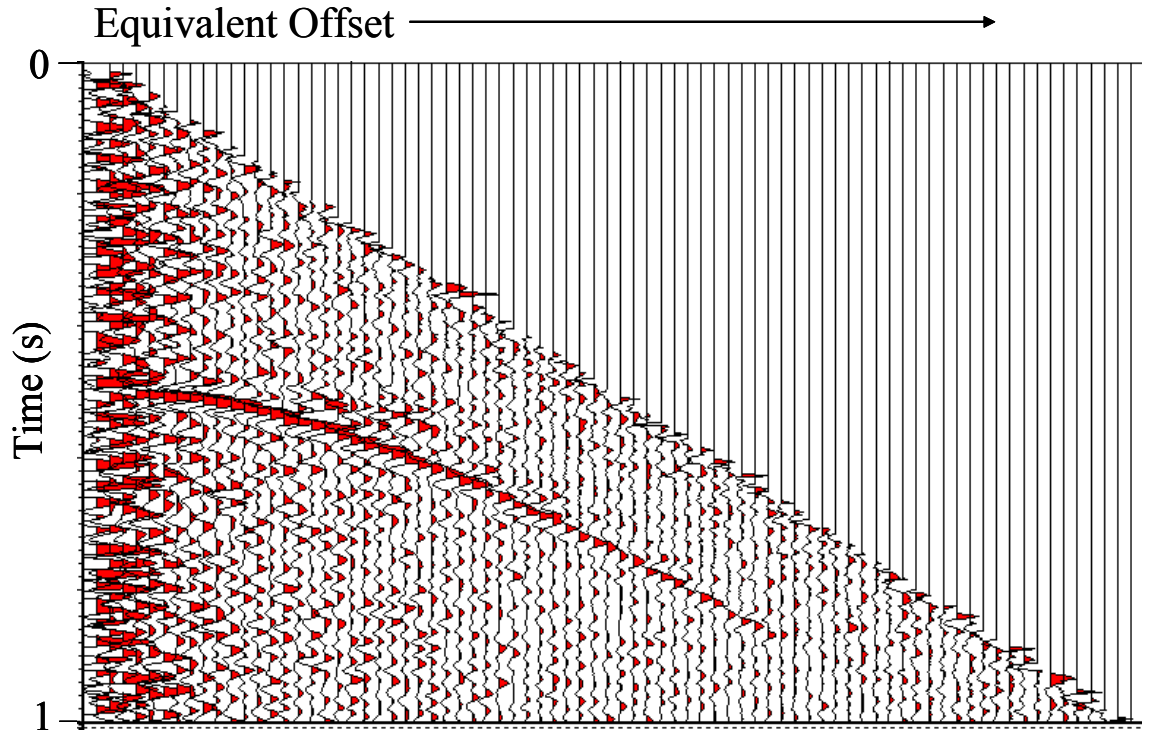
Fig. 3.3. Conventional EOCP gather located at x=1250m. No matched filtering applied. Equivalent offset shown on x-axis where dx=12.5m.

Let's now attempt to enhance the S/N ratio of the section using the pre-gather method of matched filter amplitude weighting as described in Chapter 2. This method requires calculating the angles of incidence for all x and h locations for each scatterpoint. Given the geometry in Figure 2.5, the angle subtended by the scatterpoint, α, is given by:

$$\alpha = \theta_i + \theta_r \tag{3.1}$$

where θ_i is the angle of incidence and θ_r is the angle of reflection. Using Snell's Law we obtain:

$$\frac{V_p}{V_s} = \frac{\sin\theta_i}{\sin\theta_r} \qquad (3.2)$$

Assuming that for small angles $\frac{\sin\theta_i}{\sin\theta_r} \approx \frac{\theta_i}{\theta_r}$, and upon substitution of equation (3.1)

into equation (3.2), θ_i is given as:

$$\theta_i = \frac{\alpha}{\left(1+\gamma^{-1}\right)}, \qquad (3.3)$$

where γ is the V_P/V_S ratio.

Shown in Figure 3.4 is the percent error in the approximation used in equation (3.3) where

$$\%Error = \left| \frac{\left(\frac{\sin\theta_i}{\sin\theta_r} - \frac{\theta_i}{\theta_r}\right)}{\left(\frac{\sin\theta_i}{\sin\theta_r}\right)} \right| *100 \qquad (3.4)$$

It is shown that for a V_P/V_S ratio of 2, the error in θ_i ranges from 0% at $\theta_i \sim 0°$, 5% at $\theta_i \sim 35°$, and 10% (at $\theta_i \sim 45°$).
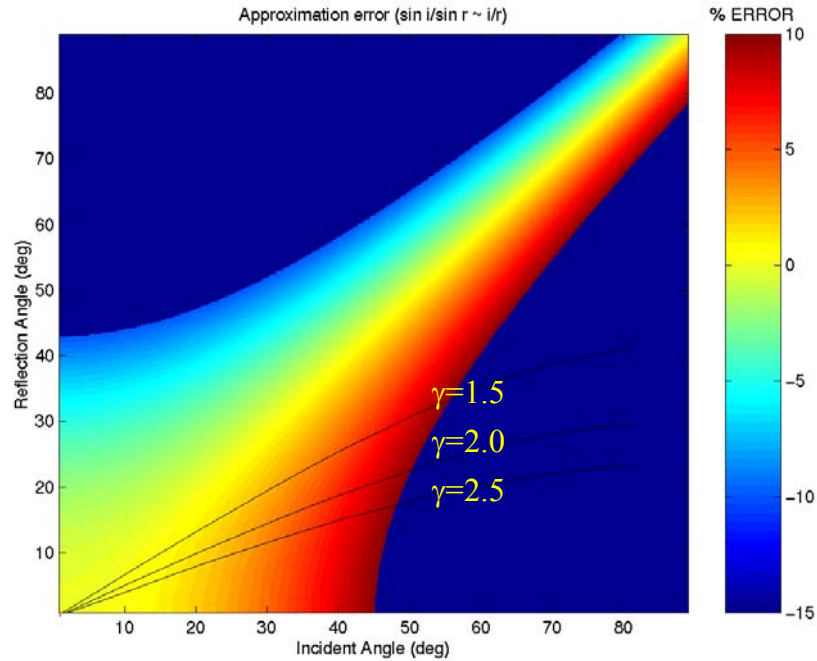
Fig. 3.4. Approximation error in assuming $\dfrac{\sin\theta_i}{\sin\theta_r} \approx \dfrac{\theta_i}{\theta_r}$.

Now that the incident angles have been estimated, and the Earth parameters of the reflection event are known, the reflection coefficient surface for all x and h pairs may be calculated for each scatterpoint. Re-gathering of the input data using the matched filter amplitude weighting produces the section found in Figure 3.5. Notice that this gather exhibits a greater S/N ratio relative to the conventional gather shown in Figure 3.3, particularly at near equivalent offsets.
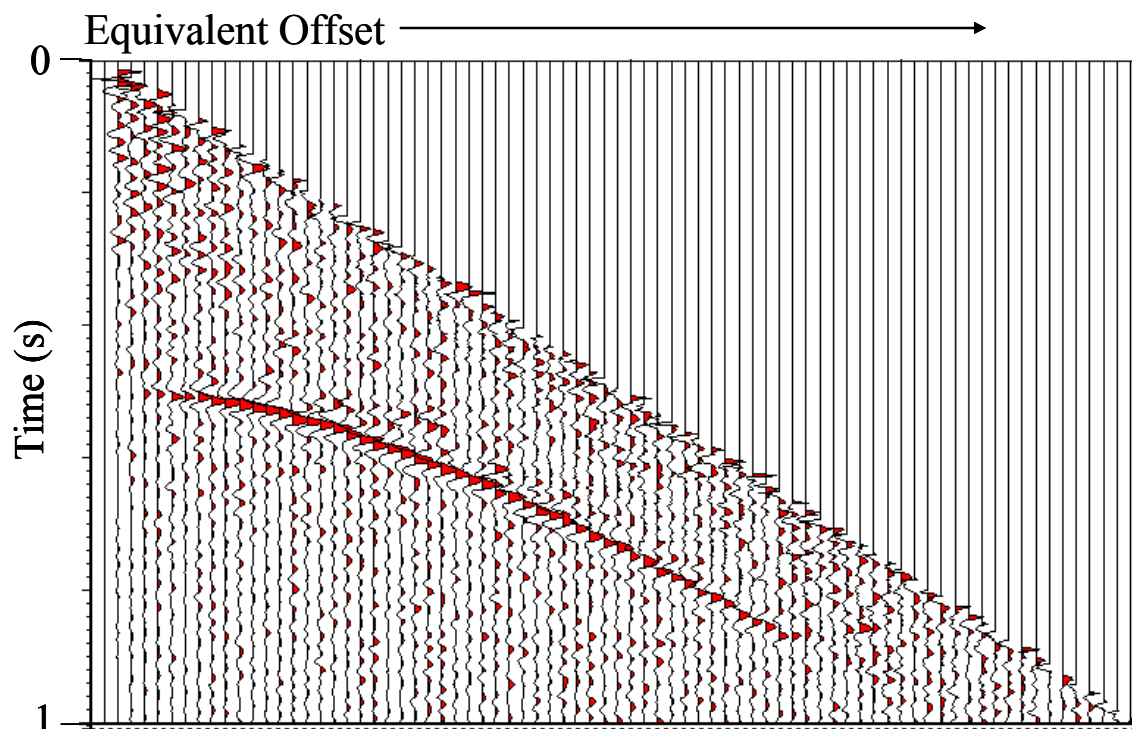
Fig. 3.5. EOCP gather located at x=1250m. Amplitudes scaled by matched filtering according to the parameters in Fig 3.1. Equivalent offset shown on x-axis, where dx=12.5m.

A comparison of the final output migrations is shown in Figure 3.6. Ten *non-matched* filtered CSP gathers, were corrected for NMO, stacked, and displayed as the first 10 traces (from left to right). The same process was repeated for the ten matched filtered gathers, and the migrated traces constitute the remaining ten traces in the figure. All traces in the figure are plotted using the same scaling factor. Notice that the use of the matched filter amplitude weighting has succeeded in increasing the S/N ratio, and thus the imaging of the output migration. The higher amplitude noise at the beginning of each trace is due to the combination of low fold and edge effects of the mute during stacking.

Conventional Migration   Matched Filter Migration
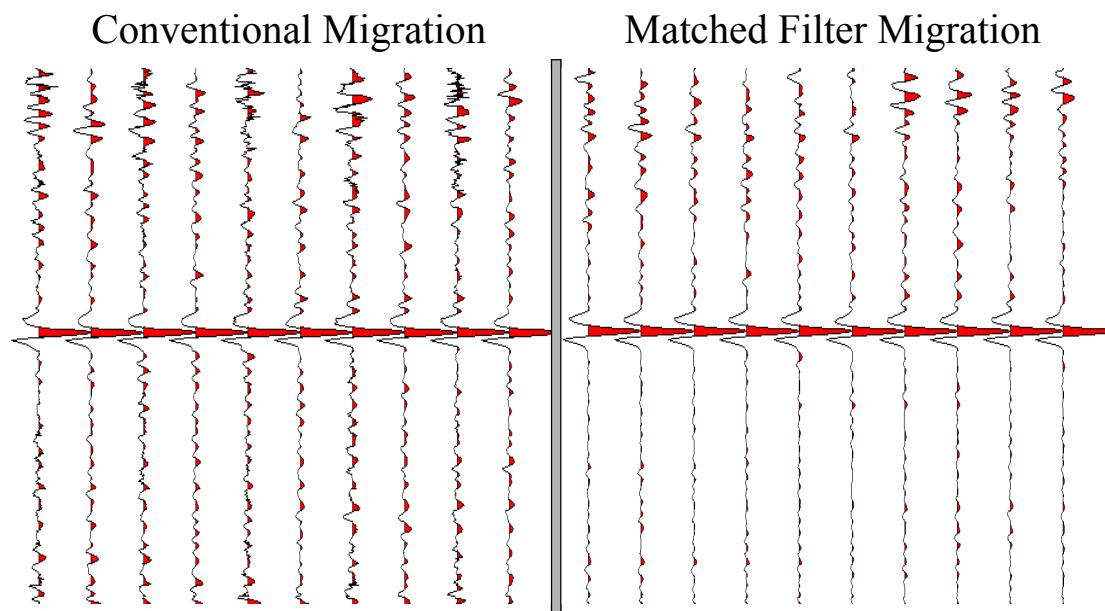
Fig. 3.6. The ten leftmost traces are NMO corrected and stacked EOCP gathers without matched filtering. The ten rightmost traces are the same migrated traces but have been matched filtered during the gathering process. Notice the increase in S/N on the macthed filtered traces.

3.3 Matched filtering of a 2D P-SV field data

In November 1997, a 2D multicomponent seismic survey was acquired by CREWES over the Encana owned Blackfoot oil field in Alberta, Canada, as shown in Figure 3.7 (Stewart *et al*., 1997). The converted wave data (P-SV) is very noisy due to the fact that well production continued throughout the acquisition of the survey. An example radial-component shot record is shown in Figure 3.8. The objective of this test is to apply the pre-gather matched filter amplitude weighting to enhance the S/N ratio, given the highly noisy data.
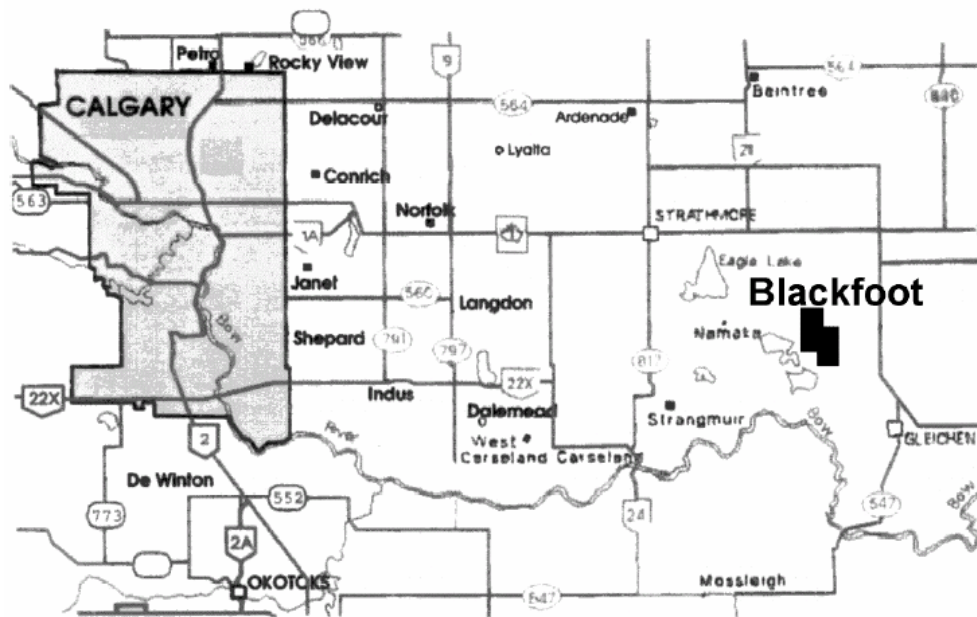
Fig. 3.7. Map showing the location of the EnCana owned Blackfoot field (from Stewart, *et al.*, 1997).
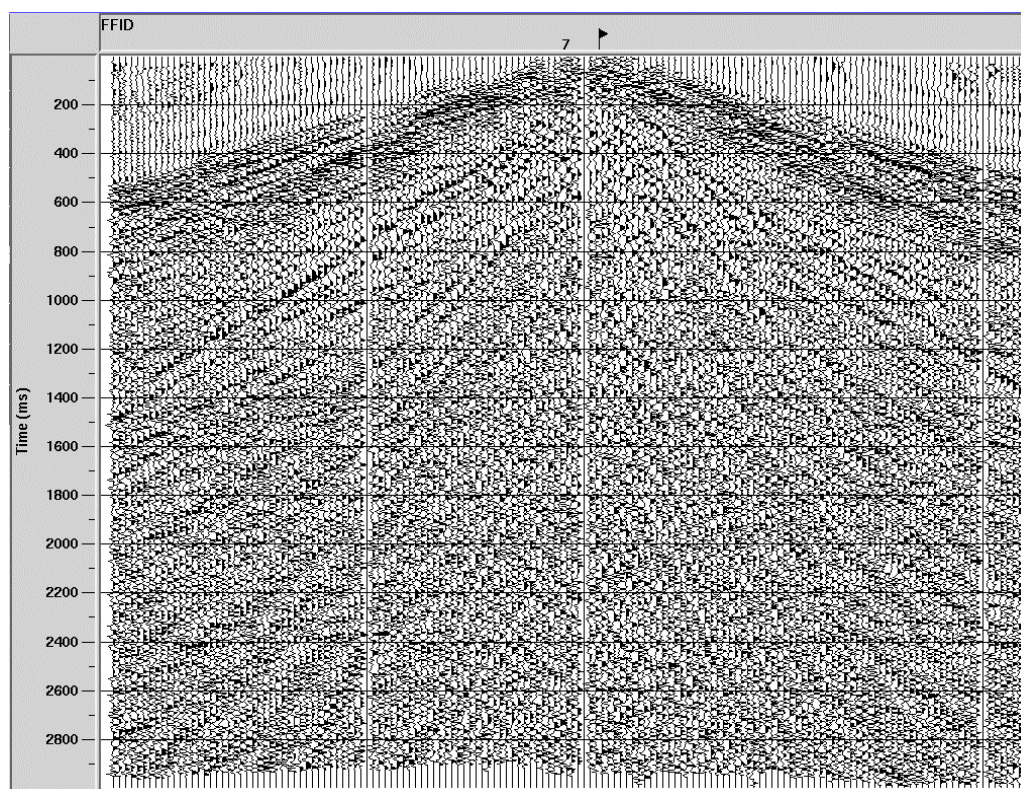
Fig. 3.8. Example Blackfoot P-SV wave shot record (radial component) with AGC.

3.3.1 Matched filter migration

Some processing of the input data has been done prior to prestack migration. The data have been binned asymptotically using a Vp/Vs ratio of 2.1 A 10-15-30-45 Hz bandpass filter has been applied. Refraction, residual, and trim statics were also applied. An existing P-P wave velocity profile of the survey was donated and used to generate the EOCP gathers. Two EOCP gathers from the same surface location are shown in Figure 3.11. A conventional gather is shown in (a) and a EOCP gather that has been formed using the pre-gather method of matched filtering is shown in (b). Elastic Earth parameters were chosen to generate a typical P-SV wave, Zoeppritz defined RC curve. The parameters and its yielding Zoeppritz RC curve are shown in Figure 3.9. Note that the absolute value of the RC curve was used for the memory function of the matched filter, as we are only concerned with the shape of the curve. Notice that (b) exhibits greater event continuity and a general increase in S/N. This effect is also evident on the semblance plots formed at the EOCP location (Figure 3.11).

NMO correction and stacking completes the migration, and a comparison of the output sections is found in Figure 3.12. Although there are still problems with the imaging, the S/N ratio of the matched filter migration is greater than that of the conventional migration. Certain events have been encircled to facilitate comparison of key improvement areas.

Processing of P-SV wave data is more involved than that of conventional P-P wave data. Blackfoot P-SV data have the added problem of the production noise greatly

obscuring reflection events, requiring special filtering techniques. For the purposes of this research, little processing was performed prior to migration to emphasize the matched filtering process.
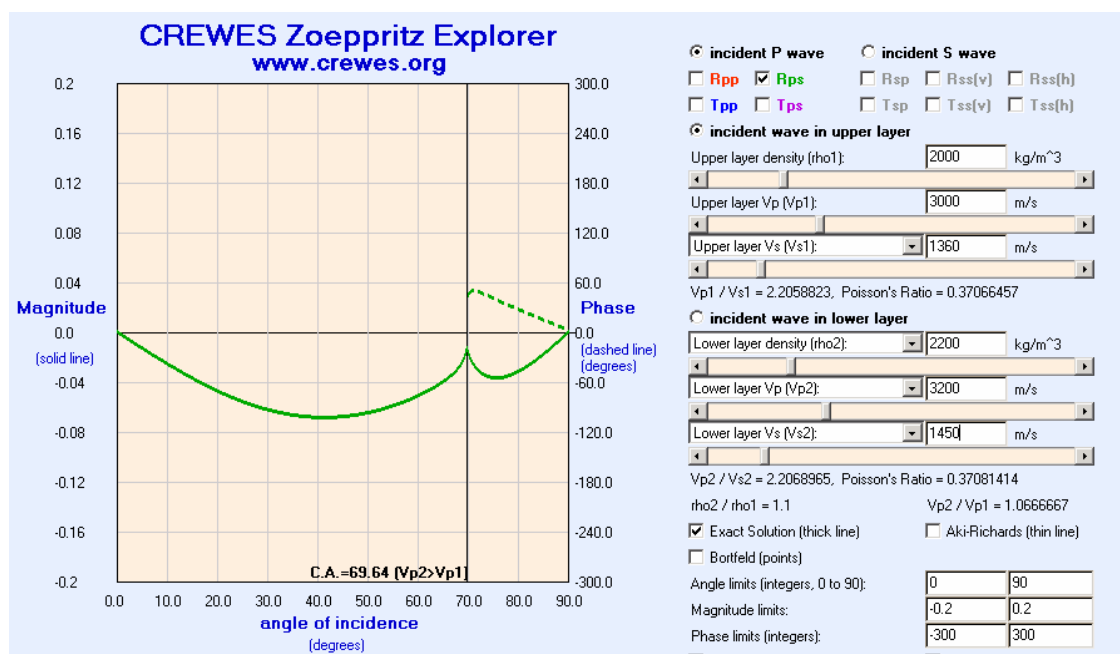
Fig. 3.9. Zoeppritz defined RC curve used in the pre-gather method of matched filtering of Blackfoot P-SV data.
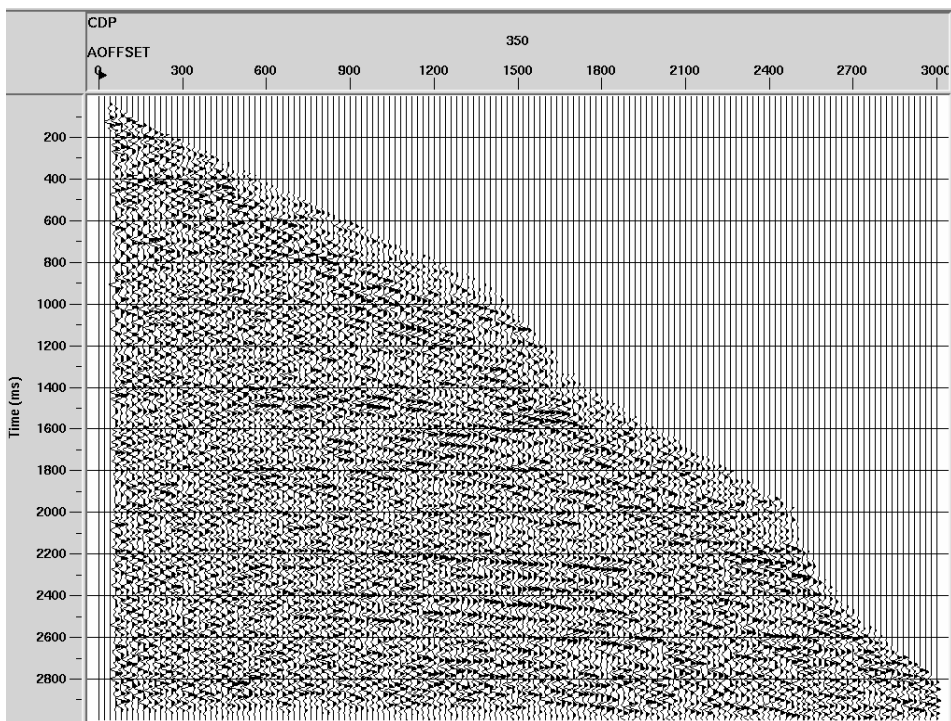
Fig. 3.10. a) Conventional EOCP gather of Blackfoot data (AGC applied).
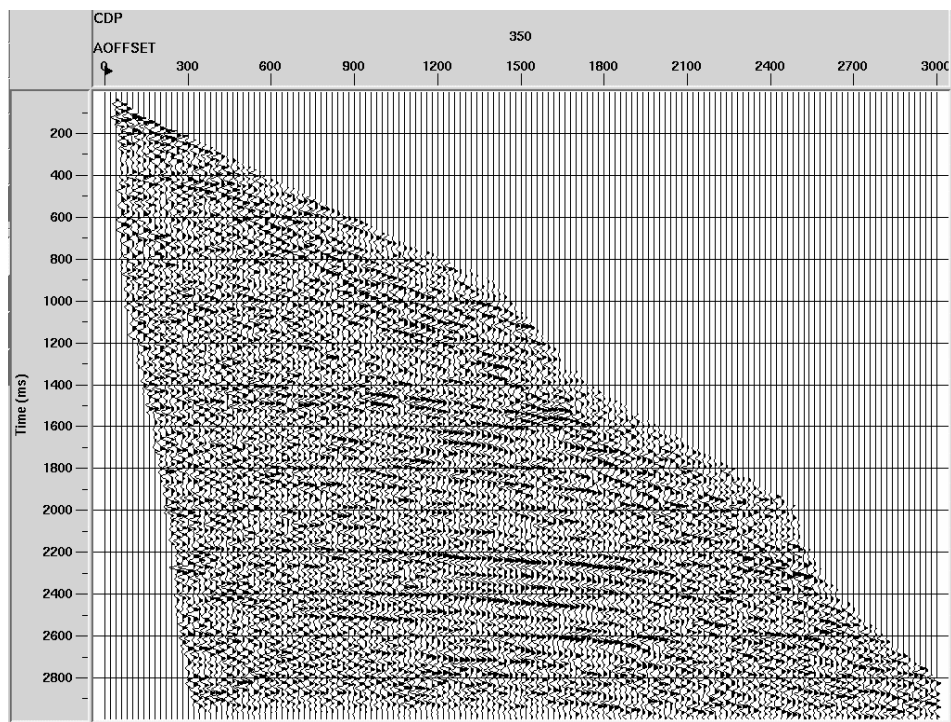
Fig. 3.10. b) Matched filter EOCP gather of Blackfoot data (AGC applied).
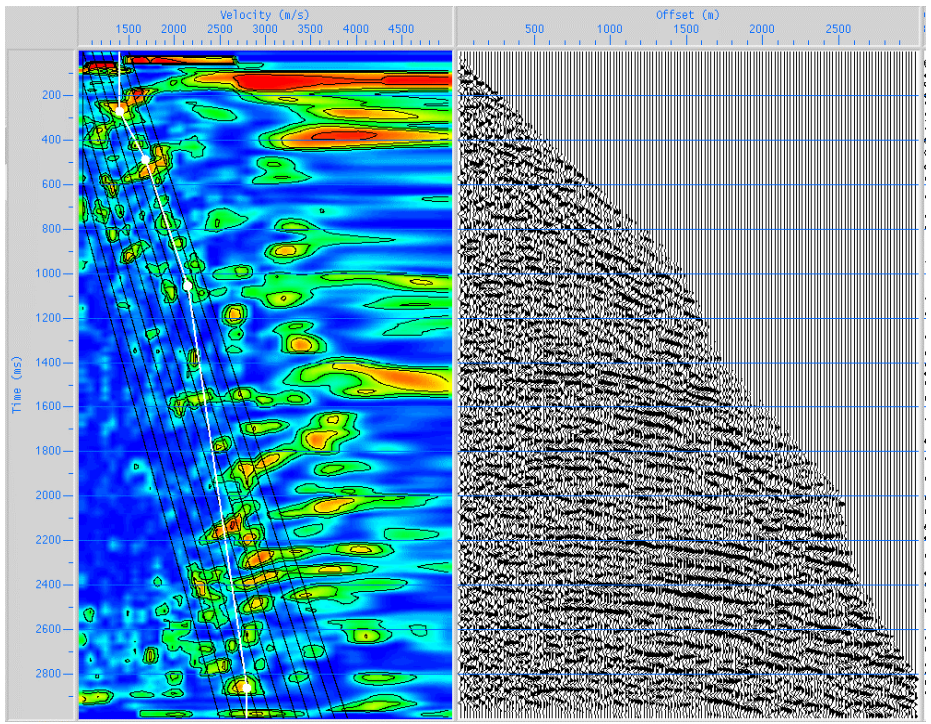
Fig. 3.11. a) Semblance plot of conventional EOCP supergather (AGC applied).
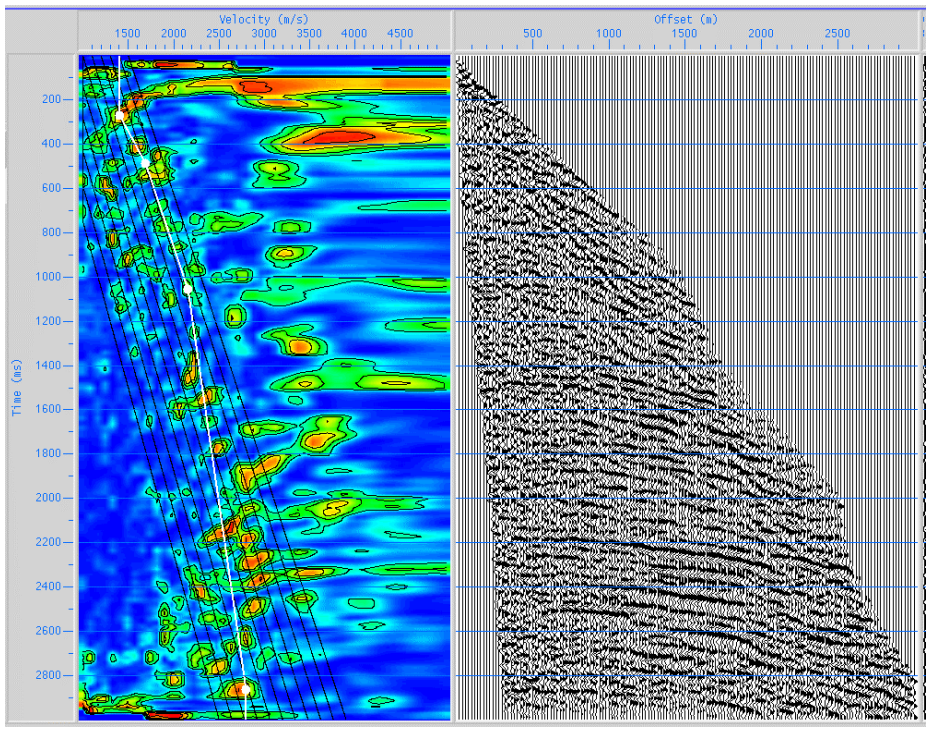
Fig. 3.11. b) Semblance plot of matched filtered EOCP supergather (AGC applied).
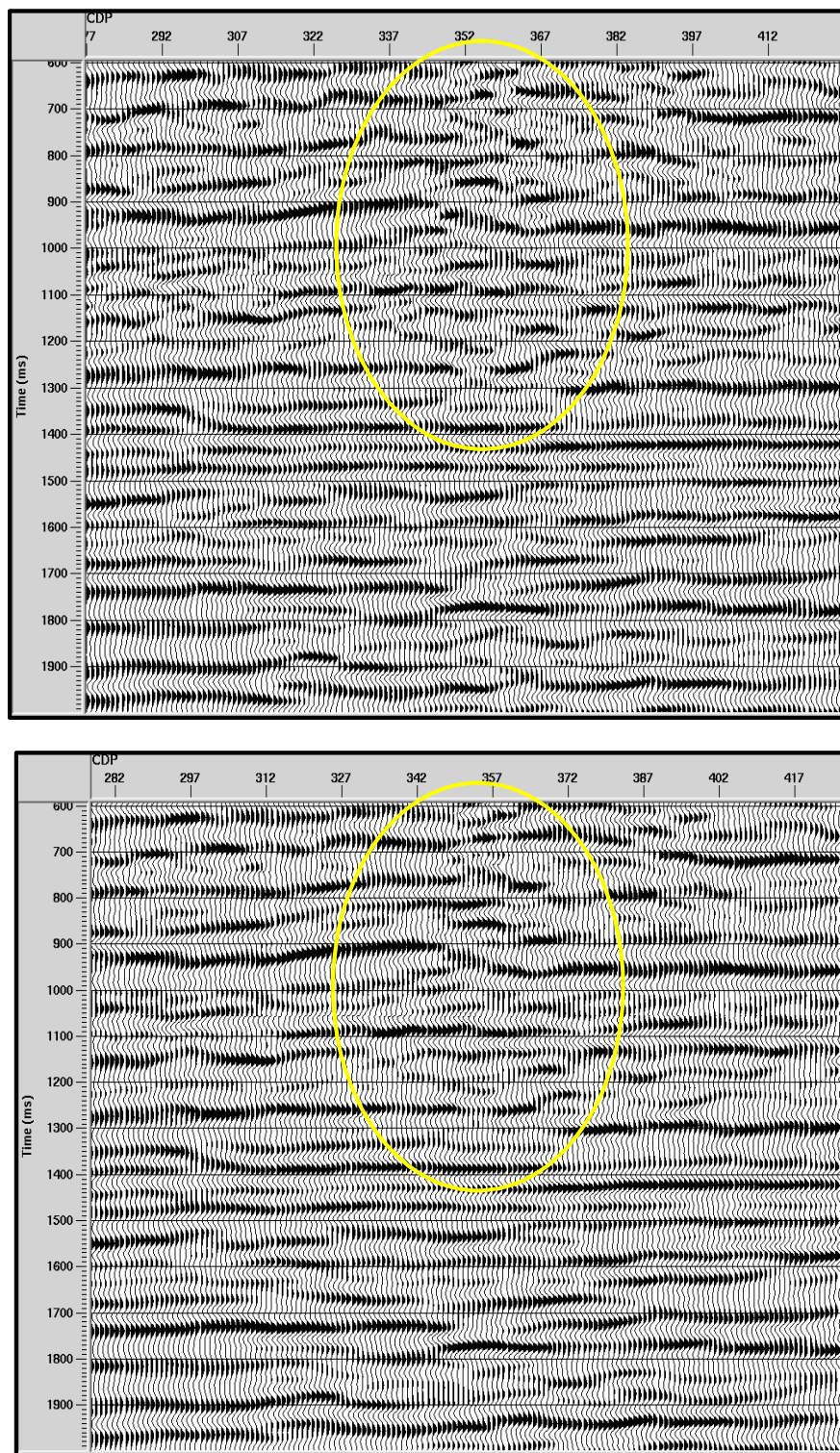
Fig. 3.12. A Conventional P-SV EOM migration (top) vs. matched filter P-SV EOM migration of Blackfoot data (bottom). Notice S/N improvement over conventional migration.

3.4 Conclusions

The pre-gather method of matched filter migration of P-SV data with an arbitrary P-SV reflection coefficient curve has been effective in increasing the SNR of the data, chiefly due to the noise cancellation at near offsets

Matched filtering results in improved velocity analysis of P-SV data.

Chapter 4: P-P wave imaging using matched filters

4.1 Introduction

In the previous chapter, it was shown that the signal-to-noise ratio of pre-stack migrated P-SV data with could be improved through matched filtering, where the memory function of the filter represents an arbitrary P-SV reflection coefficient curve that varies with angle of incidence. The following is a discussion of how matched filtering can also illuminate events that exhibit AVO behavior in conventional P-P wave data.

4.2 Synthetic data example

Consider a horizontal, four-layered Earth model and its corresponding AVO behavior as shown in Figure 4.1a. This model is loosely inspired by the reservoir in the Alba field (North Sea), where a high impedance contrast event (oil/water contact) is straddled in time by two low-impedance contrast events (top and bottom of the sand body). The oil/water contact is readily imaged in conventional processing, whereas the Class II AVO event produced from the top of the sand body pose significant imaging problems.

Shown in Figure 4.1b are the RC curves 'A' and 'C', which represent low-impedance contrast events analogous to the top and bottom sand reflections. The high-impedance contrast Event 'B' is represents a typical reflection from an oil/water contact. The objective of this study is to enhance the imaging of the Class II Event A over the imaging of the said event through conventional migration.

a)

b)   c)
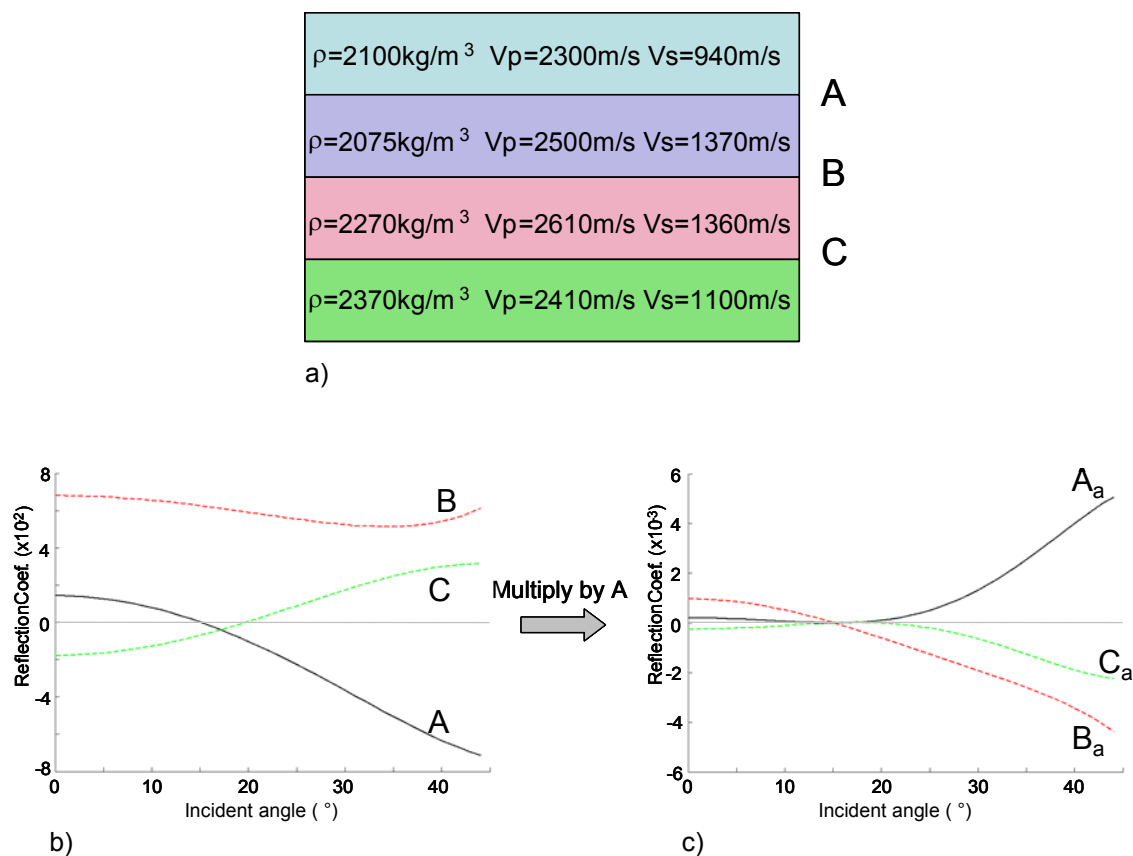
Fig. 4.1. a) The elastic Earth parameters for a four-layered Earth model. b) Reflection coefficient curves for the model. Event 'A' represents a low-impedance contrast Class II AVO anomaly, 'C' is an arbitrary low impedance event, and 'B' is a high impedance contrast event and is easily imaged. c) Effective reflection coefficient curves of a) after being matched filtered by 'A'.

Prestack data were created for this model using the same acquisition parameters as in the convert-wave model discussed in Chapter 3, where 200m separate each interface.

Random noise was added to the prestack data. An example shot record of these data is shown in Figure 4.2. Both conventional EOM, and match filter EOM were performed on the input data. Matched filter EOM requires the calculation of incident angle for each input sample. The sample is multiplied by the appropriate RC from A prior to being mapped to the EO gather. This procedure essentially multiplies all three RC curves by A, yielding the effective curves 'A$_a$', 'B$_a$', and 'C$_a$', which are shown in Figure 4.1c. The subscript 'a' implies that the original RC curve has been multiplied by coefficients of A for each angle of incidence. Equivalently, we could also say that 'a' implies that the original RC curve has been matched filtered, where the memory function of the filter represents the coefficients of A for each angle of incidence.

Matched filtering has diminished the relative difference in impedance contrast between the high-impedance event, and the low-impedance events. As event B was positive for all angles of incidence, Event B$_a$ reverses polarity near 15°, and will destructively interfere during migration. As Event A reversed polarity near 15°, A$_a$ is non-negative for all incident angles, and will constructively interfere during imaging. As the shape of C is similar to the negative of A, C$_a$ also will be better imaged than C.
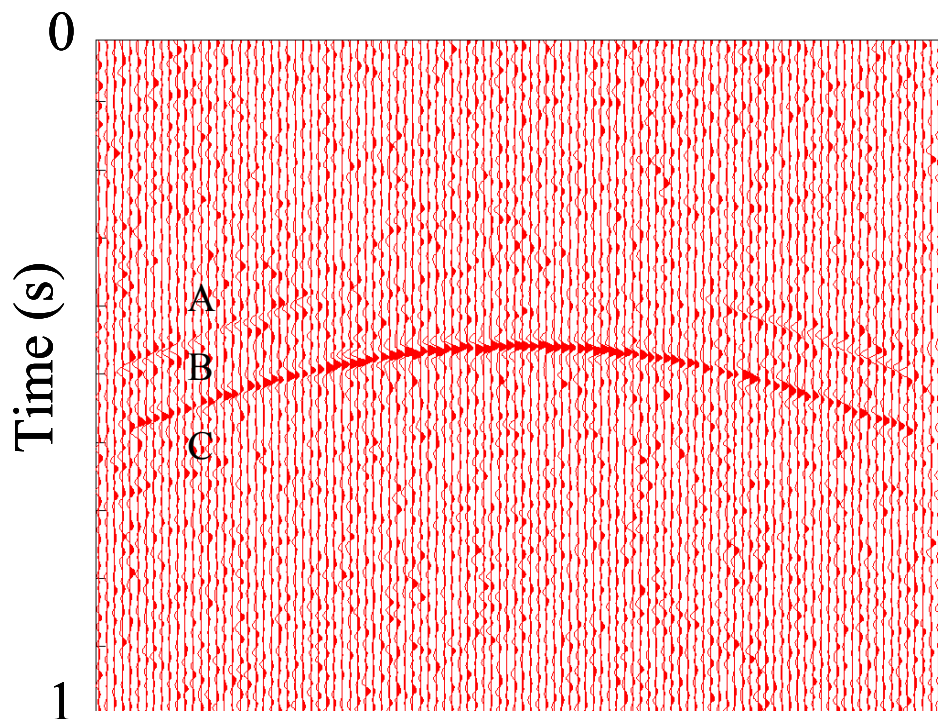
Fig. 4.2. Example synthetic shot record generated from model given in Figure 4.1 (a). Reflection events from interfaces A, B and C are labeled. Notice that events A and C are very weak relative to Event B.

Shown in Figure 4.3 are the resulting traces of 2 different migrations. Five output traces from a conventional migration without any matched filtering are shown on the left. Interface B is imaged well, however interfaces A and C are very poorly imaged. The five traces on the right are the output of a migration where the amplitudes of all input samples have been match filtered by the reflection coefficient surface defined by interface A. Notice the significant improvement in event detection of the first interface using the matched filter amplitude weighting. The detection of interface C has also improved using the 1st interface scaling.

By considering the RC curve A as 'signal' and all other RC curves as 'noise', crosscorrelation of the prestack data with A maximizes the SNR, and A_a is thus better

imaged. Since the RC curve, C, closely matches that of A, C_a is also exhibits improves imaging.
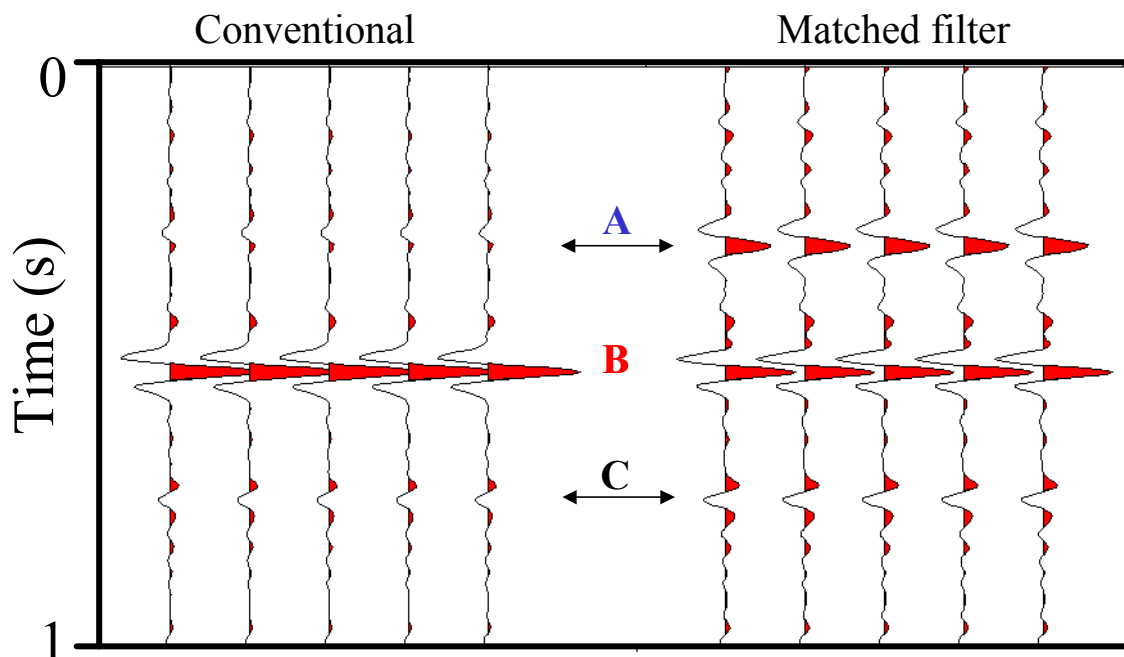
Fig. 4.3. Output traces from conventional pre-stack migration (left) compared with output migrated traces where amplitudes have been matched filtered to the reflection coefficients defined by interface A.

4.3 Imaging of P-P wave Alba Field Data

Located in the Central North Sea area, the Alba field consists of Eocene-age, high-porosity turbidite channel sands sealed by low-permeability shales. The main channel is approximately 9km long, 1.5 km wide and is found at an average subsea depth of 1900m. Thin, discontinuous, oil-saturated sands overlie the main Alba sand channel (MacLeod, 1999).

The top of the reservoir (shale-oil sand interface) gives rise to a low impedance Class II anomaly that is very difficult to image with conventional P-P wave data. As a result, a 3D ocean bottom cable (OBC) survey was conducted over the Alba field in an attempt to better image the top of the reservoir with converted-wave (P-SV) data. Chevron Petroleum donated a portion of the P-P and P-SV wave data acquired from this survey to CREWES. However, no well logs are available. In fact, the only interpretational information was found in MacLeod's paper where there is no information concerning the exact location of the reservoir. The objective of this research is to enhance the imaging of the top of the reservoir with conventional P-P wave data using the matched filter approach.

4.3.1 Overview of OBC Survey

The multicomponent OBC survey was acquired in the spring of 1998, using two 6km cables deployed on the sea bed. The cables have 1 hydrophone and 3 orthogonal geophones at each receiver location. The method of acquisition is illustrated in Figure 4.4. The cables were first deployed on the sea bed. Once in position, the source vessel shot a series of 12km lines above and parallel to the receiver cables. Between 21-23 shot lines complete the "swath". Following the acquisition of the swath, the cables are picked up and re-deployed for the next swath, and the source vessel shot another series of shot lines. The entire 3D survey was acquired using 14 swaths and a total of 3528km of shot sail lines (MacLeod, 1999).
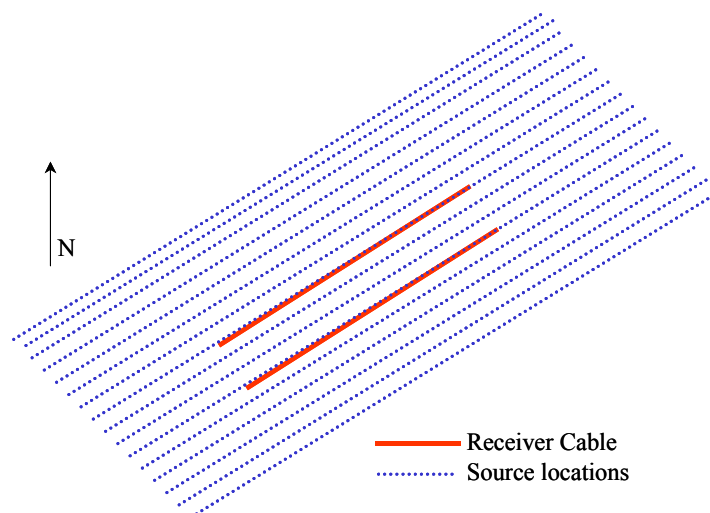
Fig. 4.4. Schematic diagram of shot lines recording an arbitrary swath.

An inline of CDP's was extracted from the prestack data (shown in Figure 4.5) to become a pseudo-2D test line, where each CDP contains traces with a range of azimuth as well as offset. CDP fold and offset distribution were two key factors in deciding which inline to extract. The latter is important because it is desirable to have as much near-offset data as possible. As the receiver positions are fixed in a 3D OBC survey the inline that best matches the location of the receiver line is the one that has the greatest amount of near-offset data. Inline 2787 was therefore extracted and chosen as the test line.
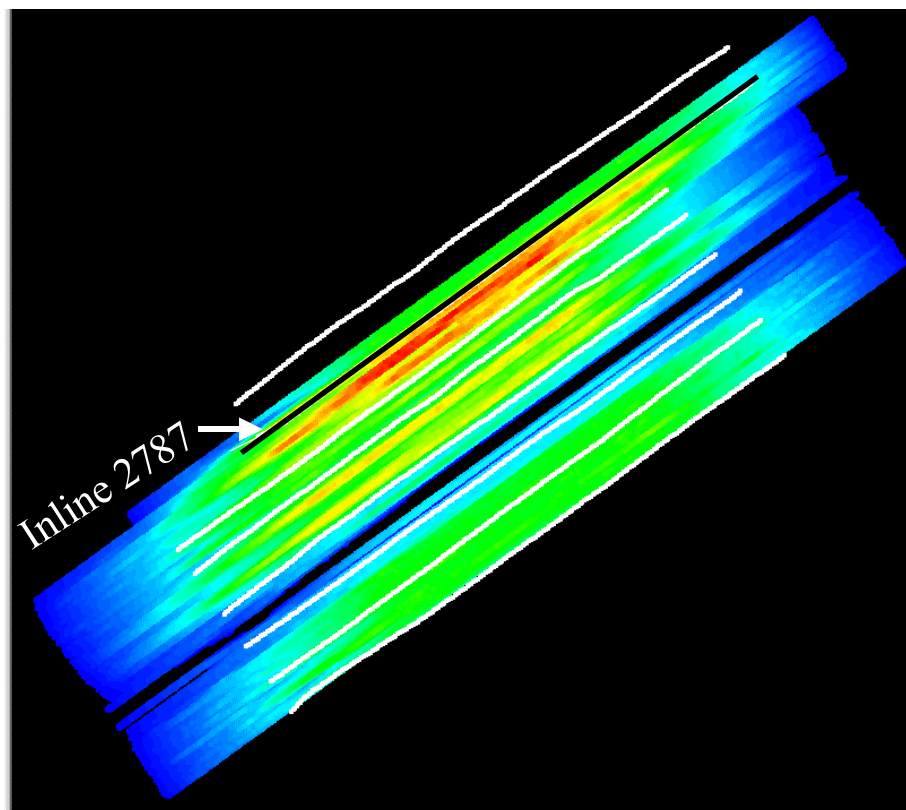
Fig. 4.5. CDP fold map. Blue=low fold, Red=High fold. White lines designate the receiver cable locations. Inline 2787 is shown in black and overlays a receiver cable.

4.3.2 Post-gather, post-stack imaging

Due to the acquisition geometry of the 3D survey, there are far more mid-offset and far-offset traces than near offset traces resulting in many empty near offset bins in a CMP gather as shown in Figure 4.6. The post-gather matched filter weighting function is most effective when all of the offset bins are full for each gather. This problem was resolved

by filling empty offset bins with a copy of the nearest possible trace, after NMO correction.
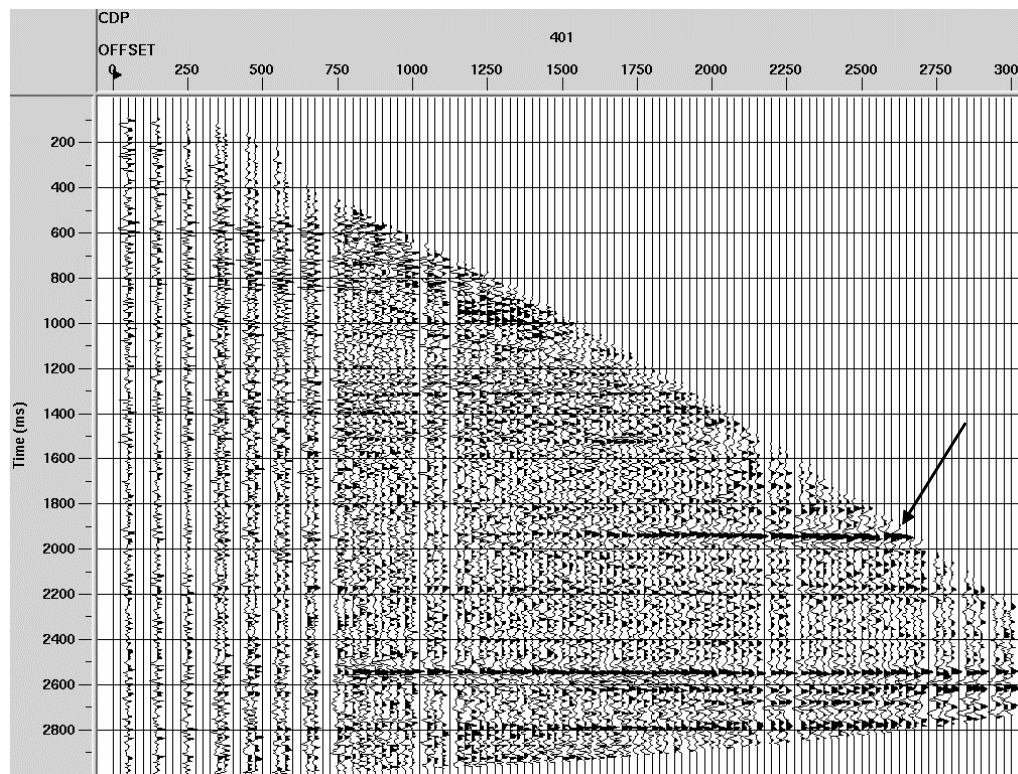
Fig. 4.6. NMO corrected CDP gather located at CDP 401. Empty near offset bins are due acquisition geometry. Notice the strong AVO anomaly at 1900ms.

Once all of the bins have been filled with data, the data were stacked, and a conventional post-stack, phase shift migration was performed and the output is shown in Figure 4.7. The CDP gather in Figure 4.6 suggests that there is an event exhibiting strong AVO behavior at ~1900ms (CDP 401). The same input CDP gathers have been matched filtered by multiplying the gather with a ramp function, as illustrated in Figure 2.18, prior to stacking. The resulting phase shift migration is found in Figure 4.8. Notice how the event ~CDP 400@ 1900ms is better imaged through matched filtering. Matched filtering appears to have cancelled much of the coherent energy in the shallower part of the

section (1000-1300ms) and has enhanced various events in the deeper part of the section (1500-2400ms). One may therefore infer that deeper section contains events with stronger AVO behavior.
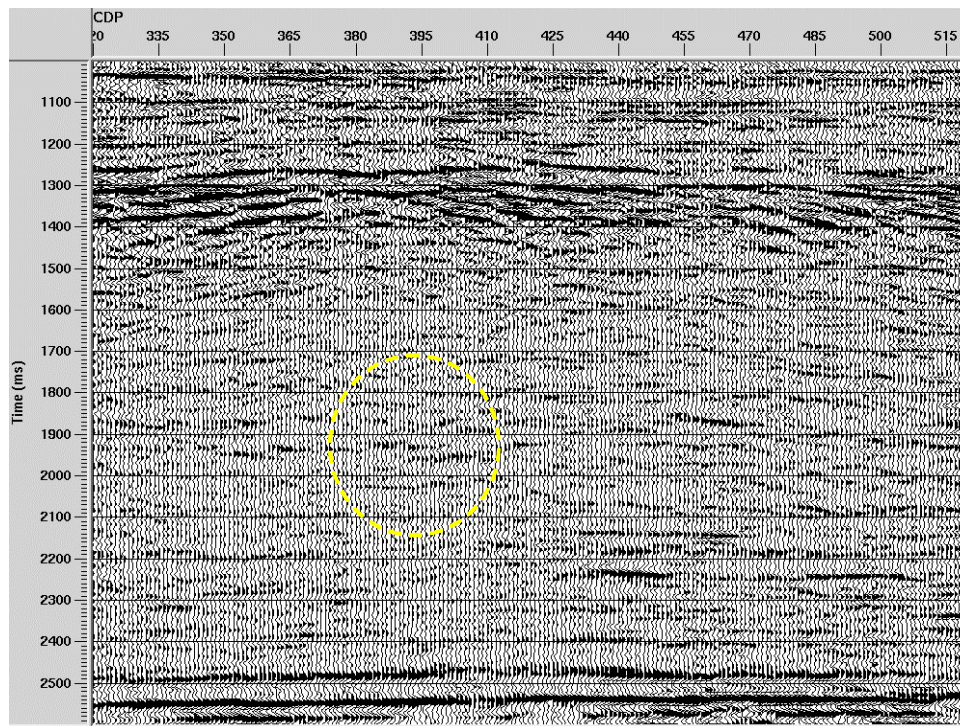
Fig. 4.7. Conventional phase shift migration of inline 2787.
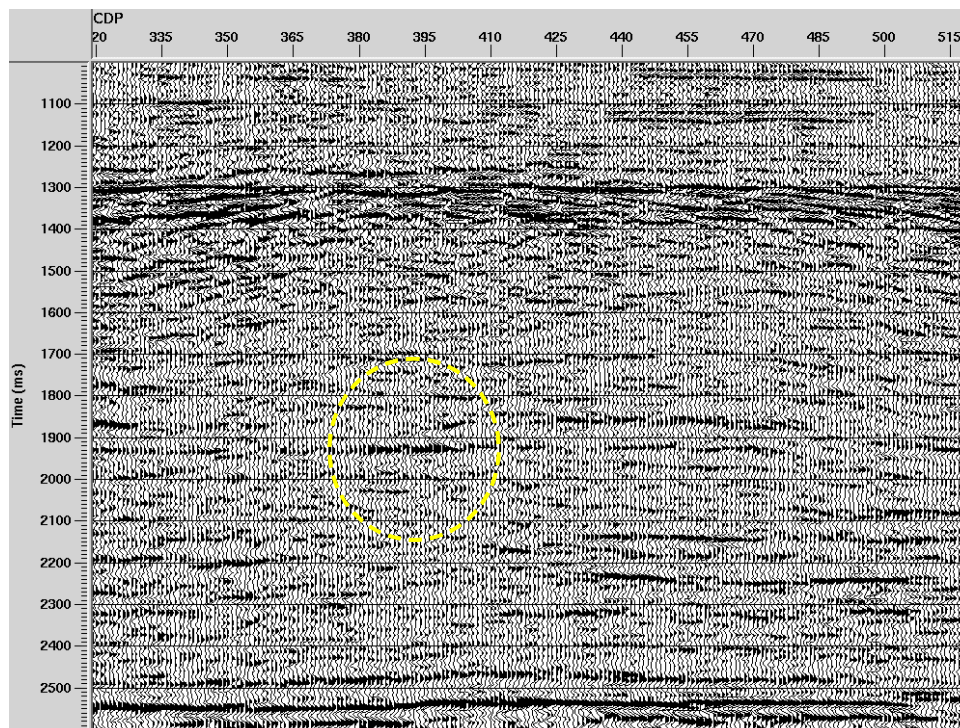
Fig. 4.8. Phase shift migration of inline 2787 after the matched filtering of CDP gathers with −1 to 1 ramp function. Notice the improvement in the imaging of the AVO event (CDP 400, ~1900ms).

4.3.3 Post-gather, pre-stack imaging

In the preceding section, CDP gathers were matched filtered with a ramp function prior to stack and post-stack migration. We can alternatively apply this ramp function to EO gathers after gathering but prior to stacking. Stacking completes the EO prestack migration.

An EO migration and a matched filtered EO migration are shown in Figures 4.9 and 4.10. In contrast with the post-stack migrated sections in Figures 4.7 and 4.8, the conventional EO pre-stack migration exhibits greater event continuity and improved SNR. More events are discernable on the pre-stack migrations. The highlighted AVO event at 1900ms is also better imaged with EO migration. In contrasting the matched filtered EOM with conventional EOM, one notices that the match filtered section shows a relative decrease in energy in the 1000-1300ms range, whereas more events are revealed in the 1400-2400ms range. One conclusion that may be inferred is that through match filtering, events that exhibit little change in AVO are suppressed, and events that have more dramatic change in AVO behavior are enhanced. If well logs from the field were available, it would be useful to generate synthetic prestack gathers using the full Zoeppritz equations. After applying a similar mute to the synthetics as to the field data, the synthetics could then be matched filtered, stacked, and then compared with the matched filtered field data. This procedure could serve as an effective QC of the matched filtering process.
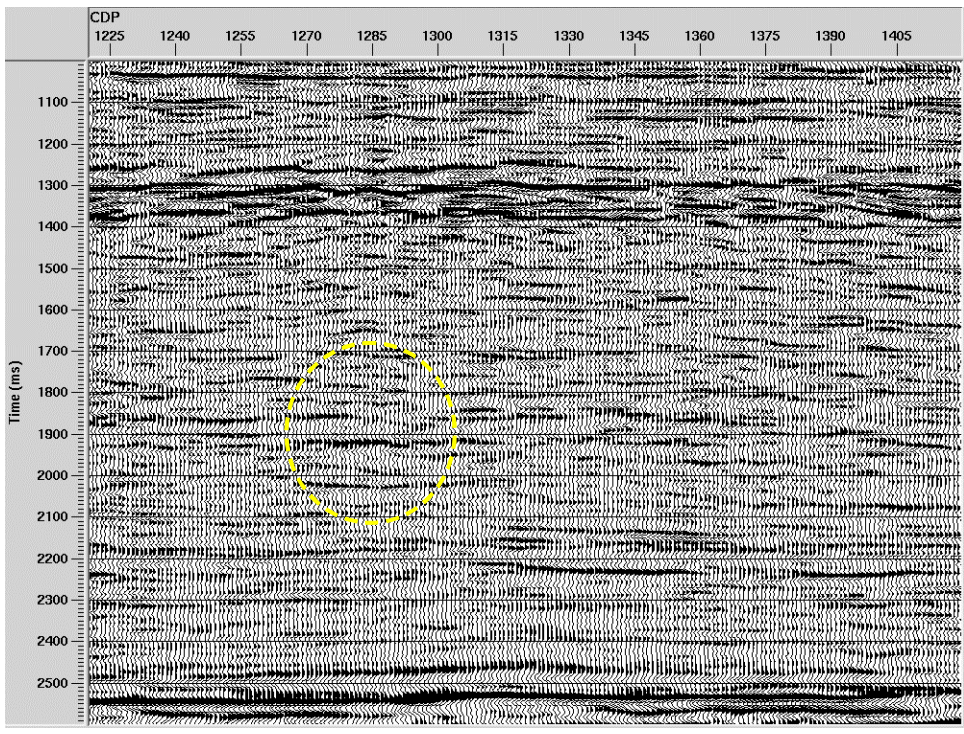
Fig. 4.9. Conventional EO migration.
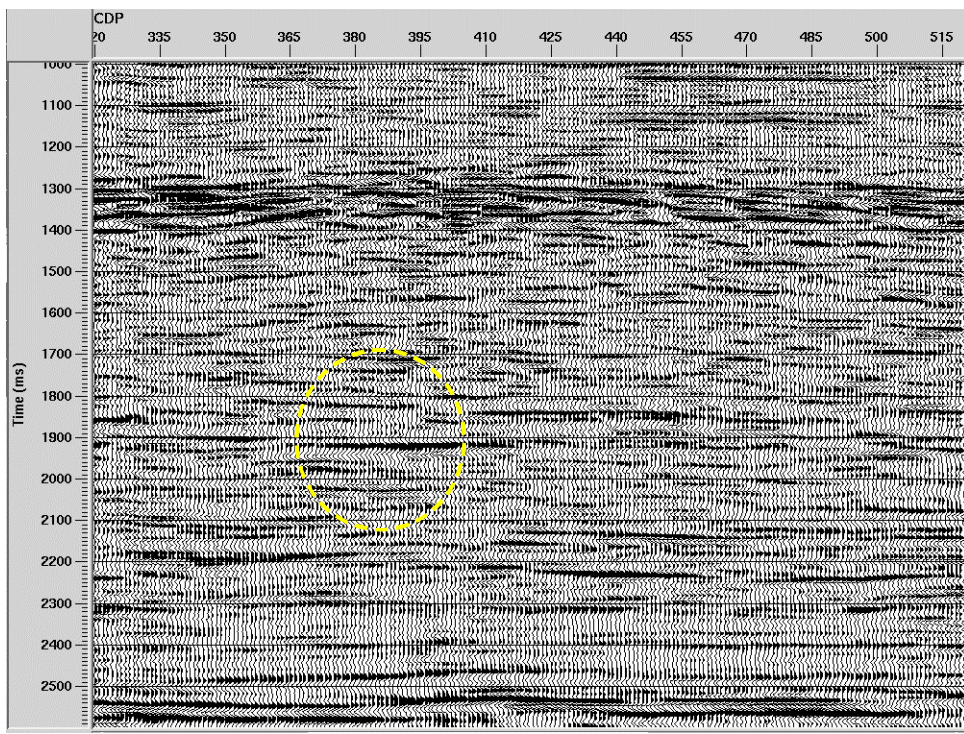
Fig. 4.10. Matched filter EO migration using post-gather method.

4.3.4 Pre-gather method of matched filtering and the absence of well logs

Attempts were made to test the pre-gather method of matched filtering to enhance the top of sand reflection event. Ideally, one may obtain the 'signal' reflection coefficient curve from modeling of the well logs. Unfortunately, no wells from the Alba field were provided for the research.

With no well logs to work with, we produced arbitrary Class II AVO response curves with Zoeppritz Explorer to use as 'signal'. However, we found that we could not obtain a better image in the zone of interest, and concluded that well data would be required to further research in this area.

4.3.5 Conclusions and comparison of routines

Testing on synthetic data revealed that the EO method of matched filtering greatly enhanced the imaging of low impedance Class II AVO events.

Conventional poststack migration vs. Matched filter poststack migration

The matched filter process has improved the detection of the highlighted AVO event at 1900ms relative to the conventional migration. Other potential AVO events have also been detected throughout the section. The shallow section (1000-1300ms) appears to have events with little AVO response relative to the deeper section.

Conventional EOM, vs. Matched filter EOM

The EOM prestack migrations appear to be superior to the respective poststack migrations in both coherence and continuity of events. The matched filtered EOM section supports the observations made on the poststack sections. The AVO event at 1900ms is better detected and the deeper section reveals events that exhibit greater coherence and continuity after matched filtering

Theoretically the matched filtered section should exhibit the following characteristics:

- Decrease in S/N ratio for reflections with flat AVO response

- Increase in S/N of other reflections that have AVO responses.

The more the AVO response deviates from a constant value, the greater the effect of this "brute force" matched filter in illuminating the event.

Chapter 5: Conclusions

The focus of this thesis is to apply matched filter theory to the imaging of seismic P-P and P-SV wave data.

A review of AVO analysis, EO migration, and matched filter theory was given in Chapter 2, and a matched filter approach to event detection in P-P and P-SV data has been proposed.

For P-P wave data, we assume that an offset trace, $s(h)$, may be expressed as a scaled version of the offset-dependent reflectivity, $r(h)$, with the addition of white noise. We then designed a matched filter whose memory function represents the reflectivity of a seismic event that we hope to enhance. Matched filtering of the data yields improved detection of the events that most closely matches the filter. Our goal was to enhance any seismic event that exhibited significant AVO behavior. We therefore chose a linear ramp function that crosses zero for the coefficients of the matched filter. Through simple synthetic data, it was shown that such a filter was successful in simultaneously canceling the energy in seismic events with a flat AVO response, and enhancing events with significant AVO response. Low impedance Class II AVO events demonstrate the most dramatic improvement in image enhancement as their AVO responses most closely match the memory function of the filter.

The matched filter method of event detection was then extended to P-SV wave data, where the filter was designed to be a near-offset noise attenuator. Since the AVO

response for an arbitrary P-SV wave reflection approaches zero as the incident angle approaches zero, the near offset data are generally noise-dominated. It was then proposed that by matched filtering P-SV wave data with an arbitrary P-SV wave AVO response curve, the noise-dominated energy at the near offsets would be suppressed relative to the signal present in the mid-offsets.

The application of the matched filter to P-SV data was tested in Chapter 3. First, a test of the noise reduction capability of the matched filter was successfully tested on a simple synthetic model. Next, the matched filter method of noise reduction was applied to Blackfoot field data. The noise reduction at near offsets improved velocity analysis and resulted in a section with events that displayed improved coherence and continuity.

Chapter 4 concerned the application of the matched filter to P-P wave data. Testing on synthetic data reveled that the EO method of matched filtering greatly enhanced the imaging of low impedance Class II AVO events. The post-gather method of match filtering was applied to Alba field data. Matched filtering of input gathers, with a linear ramp function prior to post-stack and pre-stack migrations, yielded consistent results. Both matched filtered sections showed similar areas of enhanced event detection and areas of energy cancellation relative to their respective conventional migrations.

5.1 Future work

The integration of well log data (density, compressional velocity, and shear velocity logs would be a logical next step in the proposed matched filtering process of P-P wave data.

Consider the seismic data from the Alba field. Well log data would enable one to calculate the AVO responses for the top and bottom of the reservoir interval, which could then be used as the matched filter operators. It would be of interest to compare the output matched filtered sections with the sections matched filtered using the "brute force" linear operator.

The addition of well log data to this study would also permit a comparison between the matched filtered data with the results of traditional AVO analysis, e.g. gradient, fluid, near angle, and far angle stacks.

References

Aki, K., and P. G. Richards, 1980, Quantitative seismology: Theory and methods: W. H. Freeman and Co.

Bancroft, J. C., and H. D. Geiger, 1997, Anatomy of common scatterpoint (CSP) gathers formed during equivalent offset prestack migration (EOM): CREWES Report, **9**, 28.1-28.5.

Bancroft, J. C., H. D. Geiger, and G. F. Margrave, 1998, The equivalent offset method of prestack time migration: Geophysics, **63**, 2042-2053.

Bancroft, J.C., 2000, A practical understanding of pre- and poststack migrations: Society of Exploration Geophysicists.

J. Bancroft, personal communication, 2002.

Bortfeld, R., 1961, Approximation to the reflection and transmission coefficients of plane longitudinal and transverse waves: Geophysical Prospecting, **9**, 485-503.

Castagna, J.P., and M. M. Backus, 1993, AVO analysis-tutorial and review, *in* Castagna, J. P., and M. M. Backus, eds; Offset-dependent reflectivity: Theory and practice of AVO analysis: Society of Exploration Geophysicists, 3-37.

Fatti, J. L., G. C. Smith, P. J. Vail, P. J. Strauss, and P. P. Levitt, 1994, Detection of gas in sandstone reservoirs using AVO analysis: a 3-D seismic case history using the Geostack technique: Geophysics, **59**, 1362-1376.

Hilterman, F., 1989, Is AVO the seismic signature of rock properties? : 59th Annual International Meeting, SEG, Expanded Abstracts, 559.

Hubral, P., J., Schleicher, and M. Tygel, 1996, A unified approach to 3-D seismic reflection imaging, Part 1: Basic concepts: Geophysics, **61**, 742–758.

Knott, C.G., 1899, Reflexion and refraction of elastic waves with seismological applications: Philosophical Magazine, **48**, 64-97.

Lumley, D. E., and J. F. Claerbout, 1993, Anti-aliased Kirchhoff 3-D migration: a salt intrusion example: SEG 3-D Seismic Workshop, 115–123.

MacLeod, M.K., 1999, The Alba Field ocean bottom cable seismic survey: Impact on development: The Leading Edge, **20**, 1306-1312.

Ostrander, W. J., 1982, Plane-wave reflection coefficients for gas sands at nonnormal angles of incidence: Geophysics, **49**, 1637-1648.

Ottolini, R. A., 1982, Migration of reflection seismic data in angle-midpoint coordinates: Ph.D. dissertation, Stanford University.

Richards, P.G., and C. W. Frasier, 1976, Scattering of elastic waves form depth-dependent inhomogeneities: Geophysics, **49**, 1637-1648.

Robinson, E.A., and S. Treitel, 1980, Geophysical Signal Analysis: Prentice-Hall, Inc.

Rutherford, S.R. and R. H. Williams, 1989, Amplitude-versus-offset variations in gas sands: Geophysics, **54**, 680-688.

Schneider, W. A., 1978, Integral formulation for migration in two and three dimensions: Geophysics, **43**, 49-76.

Shuey, R.T., 1985, A simplification to the Zoeppritz equations: Geophysics, **50**, 609-614.

Smith, G.C., and P. M. Gidlow, 1987, Weighted stacking for rock property estimation and detection of gas: Geophysical Prospecting, **35**, 993-1014.

Stewart, R.R., B. Hoffe, H. C. Bland, G. Margrave, E. V. Gallant, M. B. Bertram, 1997, The Blackfoot high-resolution 3-C seismic survey: design and initial results: CREWES Report **9**, 5.1-5.26.

Sun, S., 2003, The use of common scatter point gathers to detect amplitude variation with offset: M.Sc. thesis, University of Calgary.

Taner, M., and F. Koehler, 1969, Velocity spectra—Digital computer derivation and applications of velocity functions: Geophysics, **34**, 859–881.

Wang, S., J. C. Bancroft, and D. C. Lawton, 1996, Converted-wave (P-SV) prestack migration and migration velocity analysis: 66th Annual International Meeting, SEG, Expanded Abstracts, 1575-1578.

Wang, S., 1997, Three-component and three-dimensional seismic imaging: M.Sc. thesis, University of Calgary.

Zoeppritz, K., 1919, Erdbebenwellen VIIIB, On the reflection and propagation of seismic waves: Göttinger Nachrichten, I, 66-84.

Appendix A – Matrix Represenatation of the Knott-Zoeppritz Equations

Aki and Richards (1980) give the Knott-Zoeppritz equations in more convenient matrix form, and are repeated here.

The scattering matrix, Q, represents the sixteen reflection and transmission coefficients for an interface between two infinite elastic half-spaces, as shown in Figure A-1. The coefficients are represented by two letters (e.g. $\overrightarrow{PS}$), where the first letter indicates the type of incident wave, and the second letter represents the type of derived wave. The arrow pointing to the right indicates a downgoing wave, and an arrow pointing to the left indicates an upgoing wave.

Given this notation, the scattering matrix, Q, is (from Castagna and Backus, 1993)

$$Q = \begin{bmatrix} \overrightarrow{PP} & \overleftarrow{SP} & \overleftarrow{PP} & \overleftarrow{SP} \\ \overrightarrow{PS} & \overleftarrow{SS} & \overleftarrow{PS} & \overleftarrow{SS} \\ \overrightarrow{PP} & \overrightarrow{SP} & \overleftarrow{PP} & \overleftarrow{SP} \\ \overrightarrow{PS} & \overrightarrow{SS} & \overleftarrow{PS} & \overleftarrow{SS} \end{bmatrix} = P^{-1}R \tag{A-1}$$

where the matrix, P, is given by

$$P = \begin{bmatrix} -\sin\theta_1 & -\cos\phi_1 & \sin\phi_2 & \cos\phi_2 \\ \cos\theta_1 & -\sin\phi_1 & \cos\phi_2 & -\sin\phi_2 \\ 2\rho_1 V_{S1}\sin\phi_1\cos\theta_1 & \rho_1 V_{S1}(1-2\sin^2\phi_1) & 2\rho_2 V_{S2}\sin\phi_2\cos\phi_2 & \rho_2 V_{S2}(1-2\sin^2\phi_2) \\ -\rho_1 V_{P1}(1-2\sin^2\phi_1) & \rho_1 V_{S1}\sin 2\phi_1 & \rho_2 V_{P2}(1-2\sin^2\phi_2) & -\rho_2 V_{S2}\sin 2\phi_2 \end{bmatrix}$$

and matrix, *R,* is given by

$$R = \begin{bmatrix} \sin\theta_1 & \cos\phi_1 & -\sin\phi_2 & -\cos\phi_2 \\ \cos\theta_1 & -\sin\phi_1 & \cos\phi_2 & -\sin\phi_2 \\ 2\rho_1 V_{S1}\sin\phi_1\cos\theta_1 & \rho_1 V_{S1}(1-2\sin^2\phi_1) & 2\rho_2 V_{S2}\sin\phi_2\cos\phi_2 & \rho_2 V_{S2}(1-2\sin^2\phi_2) \\ \rho_1 V_{P1}(1-2\sin^2\phi_1) & -\rho_1 V_{S1}\sin 2\phi_1 & -\rho_2 V_{P2}(1-2\sin^2\phi_2) & \rho_2 V_{S2}\sin 2\phi_2 \end{bmatrix}$$

.
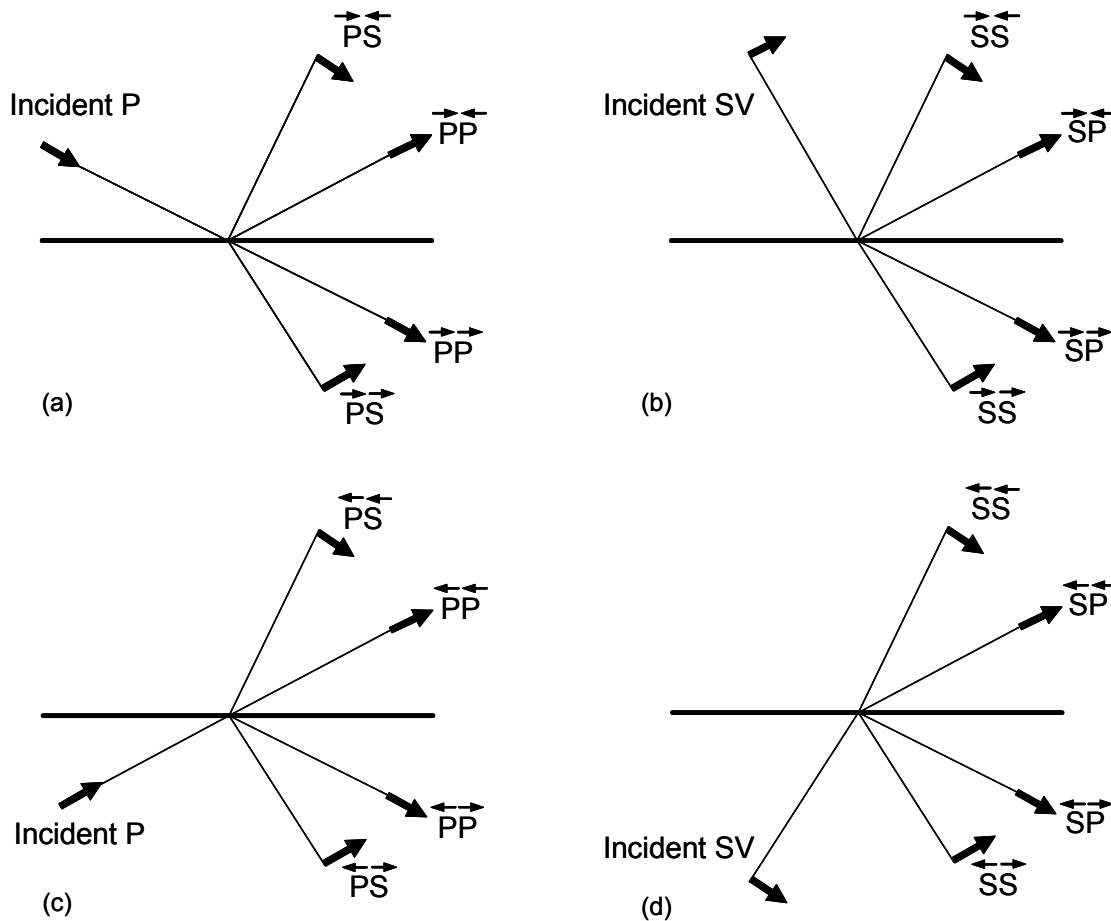
Fig. A-1. Notation of the sixteen possible reflection and transmission coefficients for *P-SV* waves at an interface between two different solid half-spaces. Short arrows show the direction of particle motion (from Aki and Richards, 1980).